



# 1 Using atmospheric observations to quantify annual biogenic carbon 2 dioxide fluxes on the Alaska North Slope

3 Luke D. Schiferl<sup>1,2</sup>, Jennifer D. Watts<sup>3</sup>, Erik J. L. Larson<sup>4</sup>, Kyle A. Arndt<sup>5,6</sup>, Sébastien C. Biraud<sup>7</sup>, Eugénie  
4 S. Euskirchen<sup>8</sup>, John M. Henderson<sup>9</sup>, Kathryn McKain<sup>10,11</sup>, Marikate E. Mountain<sup>9</sup>, J. William Munger<sup>2</sup>,  
5 Walter C. Oechel<sup>5,12</sup>, Colm Sweeney<sup>10</sup>, Yonghong Yi<sup>13,14</sup>, Donatella Zona<sup>5,15</sup>, and Róisín Commane<sup>1,16</sup>

6 <sup>1</sup>Lamont-Doherty Earth Observatory, Columbia University, Palisades, New York, USA.

7 <sup>2</sup>Harvard John A. Paulson School of Engineering and Applied Sciences, Cambridge, Massachusetts, USA.

8 <sup>3</sup>Woodwell Climate Research Center, Falmouth, Massachusetts, USA.

9 <sup>4</sup>Department of Organismic and Evolutionary Biology, Harvard University, Cambridge, Massachusetts, USA.

10 <sup>5</sup>Department of Biology, San Diego State University, San Diego, California, USA.

11 <sup>6</sup>Earth Systems Research Center, Institute for the Study of Earth, Oceans, and Space, University of New Hampshire, Durham,  
12 New Hampshire, USA.

13 <sup>7</sup>Lawrence Berkeley National Laboratory, Berkeley, California, USA.

14 <sup>8</sup>Institute of Arctic Biology, University of Alaska Fairbanks, Fairbanks, Alaska, USA.

15 <sup>9</sup>Atmospheric and Environmental Research, Inc., Lexington, Massachusetts, USA.

16 <sup>10</sup>Global Monitoring Laboratory, Earth System Research Laboratories, NOAA, Boulder, Colorado, USA.

17 <sup>11</sup>Cooperative Institute for Research in Environmental Sciences, University of Colorado, Boulder, Colorado, USA.

18 <sup>12</sup>Department of Geography, University of Exeter, Exeter, United Kingdom.

19 <sup>13</sup>Joint Institute for Regional Earth System Science and Engineering, University of California, Los Angeles, California, USA.

20 <sup>14</sup>College of Surveying and Geo-Informatics, Tongji University, Shanghai, China.

21 <sup>15</sup>Department of Animal and Plant Sciences, University of Sheffield, Western Bank, Sheffield, United Kingdom.

22 <sup>16</sup>Department of Earth and Environmental Sciences, Columbia University, New York, New York, USA.

23 *Correspondence to:* Luke D. Schiferl (schiferl@ldeo.columbia.edu)

24 **Abstract.** The continued warming of the Arctic could release vast stores of carbon into the atmosphere from high-latitude  
25 ecosystems, especially from thawing permafrost. Increasing uptake of carbon dioxide (CO<sub>2</sub>) by vegetation during longer  
26 growing seasons may partially offset such release of carbon. However, evidence of significant net annual release of carbon  
27 from site-level observations and model simulations across tundra ecosystems has been inconclusive. To address this knowledge  
28 gap, we combined top-down observations of atmospheric CO<sub>2</sub> concentrations from aircraft and a tall tower, which integrate  
29 ecosystem exchange over large regions, with bottom-up observed CO<sub>2</sub> fluxes from tundra environments and found that the  
30 Alaska North Slope is not a consistent net source or net sink of CO<sub>2</sub> to the atmosphere (ranging from −6 to +6 TgC yr<sup>−1</sup> for  
31 2012–2017). Our analysis suggests that significant biogenic CO<sub>2</sub> fluxes from unfrozen terrestrial soils, and likely inland waters,  
32 during the early cold season (September–December) are major factors in determining the net annual carbon balance of the  
33 North Slope, implying strong sensitivity to the rapidly warming freeze-up period. At the regional level, we find no evidence  
34 for previously reported large late cold season (January–April) CO<sub>2</sub> emissions to the atmosphere during the study period.  
35 Despite the importance of the cold season CO<sub>2</sub> emissions to the annual total, the interannual variability of the net CO<sub>2</sub> flux is  
36 driven by the variability in growing season fluxes. During the growing season, the regional net CO<sub>2</sub> flux is also highly sensitive  
37 to the distribution of tundra vegetation types throughout the North Slope. This study shows that quantification and



38 characterization of year-round CO<sub>2</sub> fluxes from the heterogeneous terrestrial and aquatic ecosystems in the Arctic using both  
39 site-level and atmospheric observations is important to accurately project the earth system response to future warming.

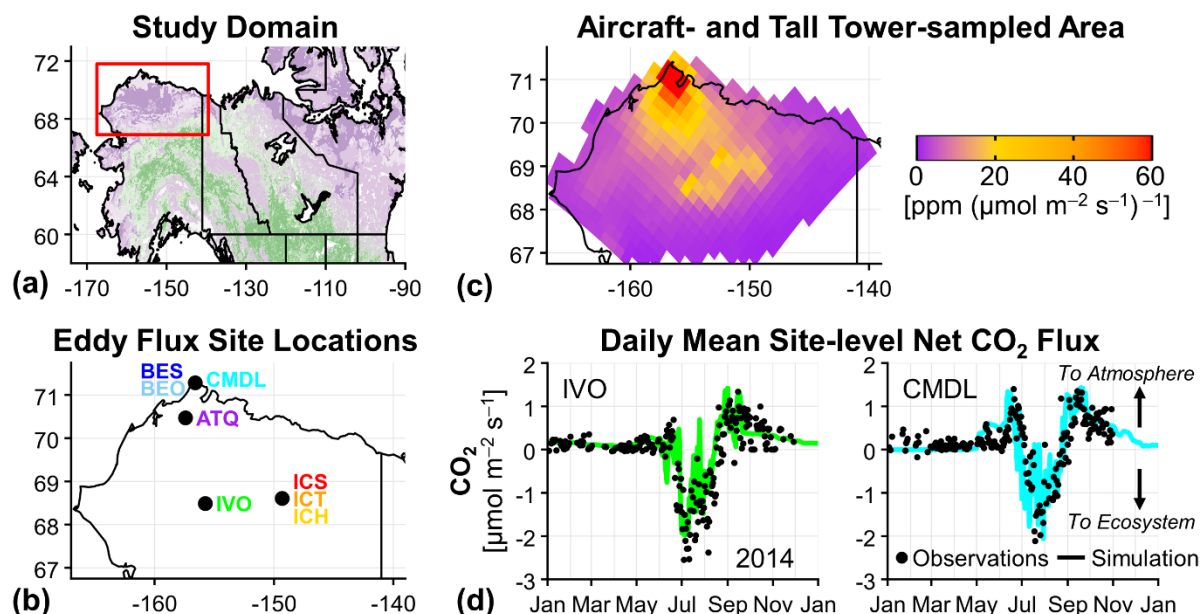
## 40 **1 Introduction**

41 The Arctic surface air temperature is warming at twice the rate of the global average (Box et al., 2019; Meredith et al., 2019).  
42 Continued thawing of Arctic permafrost has the potential to release vast stores of carbon into the atmosphere, thereby further  
43 accelerating warming (Schoor et al., 2015; Hugelius et al., 2014). In the biosphere, the net CO<sub>2</sub> flux is the balance between  
44 uptake of CO<sub>2</sub> by vegetation through photosynthesis (negative net CO<sub>2</sub> flux indicates removal from the atmosphere) and release  
45 of CO<sub>2</sub> into the atmosphere by plant and microbial respiration (positive net CO<sub>2</sub> flux indicates a source to the atmosphere).  
46 Arctic growing seasons are short (~3 months), and the long, cold season dominates the seasonal cycle. The transition between  
47 the growing and cold seasons is marked by the soil zero-curtain period, when belowground temperatures of the active layer  
48 above frozen permafrost remain near freezing; the active layer is insulated by snow and ice at the surface and warmed by the  
49 latent heat release of freezing water (Outcalt et al., 1990). During the zero-curtain period, soil respiration can remain active in  
50 deeper soils for weeks to months after the end of the growing season (Zona et al., 2016; Romanovsky and Osterkamp, 2000).  
51 As the climate warms, the active layer above permafrost deepens, thawed soils become wetter, a larger volume of soil remains  
52 unfrozen for a longer period of time, and the duration of the zero-curtain period plays an increasingly important role in  
53 determining the net carbon exchange in Arctic ecosystems (Kim et al., 2012; Arndt et al., 2019). Recent work has shown a  
54 significant cold season source of CO<sub>2</sub> from Arctic ecosystems, including more than 70% increase in October–December CO<sub>2</sub>  
55 concentration enhancements in the past 40 years, consistent with an increase in cold season respiration, which is not well  
56 represented in earth system models (Commane et al., 2017; Natali & Watts et al., 2019). Neglecting these processes could lead  
57 to large underestimation of CO<sub>2</sub> emissions, biasing current and future climate projections.

58 Tundra ecosystems, characterized by frozen soils covered in low shrubs, sedges, grasses, and mosses, make up  
59 approximately 50% of the Arctic landscape (Raynolds et al., 2019). Lacking trees, the magnitude of net CO<sub>2</sub> uptake in tundra  
60 during the growing season is relatively small and may be offset by emissions from respiration that can continue well into the  
61 cold season (Watts et al., 2021). In the past, year-round CO<sub>2</sub> flux measurements from tundra ecosystems were rare due to  
62 difficulties in maintaining instrumentation under remote and extreme cold conditions (Euskirchen et al., 2017; Kittler et al.,  
63 2017; Goodrich et al., 2016). Long-term year-round CO<sub>2</sub> concentration measurements have been made in the Arctic at a small  
64 number of tall towers, which have been situated to sample clean marine air off the ocean (Jeong et al., 2018; Worthy et al.,  
65 2009). While aircraft provide greater spatial coverage over land than these towers, they tend to operate for short durations, and  
66 their temporal coverage is limited by weather and visibility during the cold season (Chang et al., 2014; Commane et al., 2017;  
67 Miller et al., 2016). However, the recent increase in availability of observations of gas fluxes and concentrations within a  
68 particular tundra region, the Alaska North Slope (Fig. 1a), is making it possible to better conduct year-round multi-scale



69 assessments of tundra ecosystems, with the aim of improving our understanding of CO<sub>2</sub> sink/source activity and carbon budgets  
70 in these environments.



71  
72 **Figure 1.** Alaska North Slope study region, eddy flux site locations, area sampled by aircraft and tower, and example results from the eddy  
73 flux site measurement-model comparison. (a) North Slope region (red box) within Alaska and northwestern Canada. Tundra areas shown in  
74 purple and boreal forest areas shown in green (Luus et al., 2017). (b) Location of eddy flux measurement sites on the Alaska North Slope  
75 used in this analysis. (c) Ten-day WRF-STILT footprints used to sample CO<sub>2</sub> flux models, summed for all aircraft and tall tower CO<sub>2</sub>  
76 observations used in this analysis. Colors represent values greater than 0 and are saturated at 60 ppm ( $\mu\text{mol m}^{-2} \text{s}^{-1}$ )<sup>-1</sup>. Maximum value near  
77 Utqiagvik, Alaska is 324 ppm ( $\mu\text{mol m}^{-2} \text{s}^{-1}$ )<sup>-1</sup>. (d) Timeseries of observed (black dots) and simulated (colored lines) site-level daily mean  
78 net CO<sub>2</sub> flux for 2014 at IVO (left) and CMDL (right) eddy flux measurement sites, where site-level TVPRM net CO<sub>2</sub> flux simulations are  
79 driven by NARR meteorology and the CSIF SIF product. Positive net CO<sub>2</sub> flux values indicate CO<sub>2</sub> fluxes into the atmosphere throughout  
80 this study. A comparison for all eight eddy flux sites is provided in Fig. S1 in Supplement.

81 Currently, observations and models do not agree on the sign of the annual net CO<sub>2</sub> flux across the Alaska North Slope  
82 region. Site-level measurements and atmospheric observations suggest this region is a net CO<sub>2</sub> source (Commane et al., 2017;  
83 Oechel et al., 2014; Euskirchen et al., 2017). However, a comparison of process-based models of the North Slope found large  
84 variability in the sign and magnitude of the net CO<sub>2</sub> flux with an approximately neutral regional annual net CO<sub>2</sub> flux multi-  
85 model mean of  $-3.5 \pm 67 \text{ TgC yr}^{-1}$  (Fisher et al., 2014). In a more recent study, Tao et al. (2021) found an annual net CO<sub>2</sub> flux  
86 range of  $-9$  to  $12 \text{ TgC yr}^{-1}$  for the years 2010–2016, with only 2014 being an annual net CO<sub>2</sub> source. Extrapolating from site-  
87 level CO<sub>2</sub> flux measurements to regional budgets is difficult due to the extreme heterogeneity of tundra ecosystems in the  
88 North Slope and a lack of spatial and seasonal representativeness by existing flux monitoring sites (Pallandt et al., 2022).

89 In this study, we compare *bottom-up* flux estimates with *top-down* atmospheric observations from aircraft and a tall  
90 tower using an integrated modeling approach to quantify the CO<sub>2</sub> budget sign and magnitude of the Alaska North Slope. Our  
91 framework first applies a bottom-up approach to understand Arctic tundra ecosystem CO<sub>2</sub> fluxes, constrained by site-level  
92 observations, using an empirical model ensemble of CO<sub>2</sub> fluxes derived from eddy flux measurements representing varied



93 tundra ecosystems within the region. We then apply top-down information gained from regional CO<sub>2</sub> concentration  
94 observations measured by a tall tower and aircraft, which sample the atmosphere-biosphere exchange throughout the Alaska  
95 North Slope, to evaluate the range of potential CO<sub>2</sub> fluxes identified by the bottom-up model ensemble for 2012–2017. This  
96 evaluation also identifies the ecosystem parameterizations, vegetation distributions, and environmental drivers that best  
97 characterize the observed spatial and temporal distribution of biogenic CO<sub>2</sub> in the atmosphere across the region. By developing  
98 regional CO<sub>2</sub> budgets constrained by both atmospheric observations and ecosystem environmental responses, we can better  
99 project how Arctic tundra ecosystems will respond to climate change on annual and decadal timescales.

## 100 **2 Materials and methods**

### 101 **2.1 Observed CO<sub>2</sub> concentrations and fluxes on the Alaska North Slope**

#### 102 **2.1.1 Atmospheric CO<sub>2</sub> concentration observations**

103 We use a suite of CO<sub>2</sub> concentration observations from various sources on the North Slope for our analysis. The United States  
104 (US) National Oceanic and Atmospheric Administration (NOAA) Barrow Atmospheric Baseline Observatory (BRW) tall  
105 tower near Utqiagvik, Alaska has made continuous in situ CO<sub>2</sub> concentration measurements since 1973 (Sweeney et al., 2016).  
106 The US Department of Energy (DOE) Atmospheric Radiation Measurement Climate Research Facility Airborne Carbon  
107 Measurements V (ARM-ACME V) airborne campaign measured CO<sub>2</sub> concentrations sub-weekly from June to September  
108 2015 over the North Slope (Biraud et al., 2016; Tadić et al., 2021). The US National Aeronautics and Space Administration  
109 (NASA) Arctic-Boreal Vulnerability Experiment (ABoVE) Arctic Carbon Atmospheric Profiles (Arctic-CAP) airborne  
110 campaign flew throughout Alaska and northwestern Canada approximately every month from May to November 2017  
111 (Sweeney and McKain, 2019; Sweeney et al., 2022). CO<sub>2</sub> concentration observations from the NASA Carbon in Arctic  
112 Reservoirs Vulnerability Experiment (CARVE) flights for 2012–2014 are incorporated into the Commane et al. (2017)  
113 optimized CO<sub>2</sub> fluxes used in our analysis below. The NOAA/US Coast Guard collaborative Alaska Coast Guard (ACG)  
114 flights have also made aircraft CO<sub>2</sub> concentration measurements in the region, but these coastal flights observe only limited  
115 spatial coverage of the North Slope, and we do not use them here.

116 For the NOAA BRW tower, we use hourly CO<sub>2</sub> concentration observations with wind direction from the land (135°–  
117 202.5° clockwise w.r.t. north) and ocean sectors (0°–45°), avoiding Utqiagvik anthropogenic activity, with wind speed > 2.5  
118 m s<sup>-1</sup> (Fig. S2) (Commane et al., 2017; Sweeney et al., 2016). We only use land sector observations from the cold season  
119 (defined here as September–April) since seasonal wind patterns do not favor transport from those directions during the growing  
120 season (defined here as May–August). For the ARM-ACME V and ABoVE Arctic-CAP aircraft campaign observations, we  
121 group averaged sampling points into 50 m vertical bins after removing data influenced by biomass burning events, indicated  
122 by elevated or varying carbon monoxide (CO) concentrations. These sampling points correspond to the available Lagrangian  
123 atmospheric transport modeling system simulations (WRF-STILT (Henderson et al., 2015), see below): ARM-ACME V points



124 are calculated every 50 m vertically below 1 km, every 100 m vertically above 1 km, and every 10 km horizontally from 1 s  
125 observations, and ABoVE Arctic-CAP points are matched every 20 s from averaged 10 s observations. To ensure these points  
126 observe the Alaska North Slope, we only use points with at least 70% of the total 10-day WRF-STILT simulated surface  
127 influence occurring in our regional domain.

### 128 **2.1.2 Eddy covariance CO<sub>2</sub> flux tower observations**

129 We also use up to five years (2013–2017) of year-round observations of net CO<sub>2</sub> flux from eight eddy covariance tower sites  
130 (for 32 total site-years) representing an array of tundra ecosystems throughout the Alaska North Slope (Figs. 1b, S1, Table S1  
131 in Supplement). These half-hourly eddy flux measurements of net CO<sub>2</sub> flux are not gap-filled to avoid introducing additional  
132 uncertainties. Three of the sites are located near Imnavait Creek along a wetness gradient from valley to hilltop: wet sedge  
133 tundra (ICS), moist acidic tussock tundra (ICT) and dry heath tundra (ICH) (Euskirchen et al., 2017, 2012). The other sites  
134 include tussock tundra at Iivotuk (IVO), wet polygonised tundra at Atqasuk (ATQ), and three sites near Utqiagvik: wetland  
135 tundra (BES), wet polygonised tundra (BEO), and moist tundra (CMDL) (Zona et al., 2016; Arndt et al., 2020).

### 136 **2.2 Observed atmospheric CO<sub>2</sub> concentration enhancement calculation**

137 We calculate the observed *top-down* atmospheric CO<sub>2</sub> concentration enhancement ( $\Delta\text{CO}_2$ ) for the North Slope region for every  
138 land-sector hour at the NOAA BRW tower and for every 50 m of vertical distance transited during the airborne campaigns  
139 (ARM-ACME V, ABoVE Arctic-CAP). The observed  $\Delta\text{CO}_2$  [units: ppm] generated by the North Slope ecosystem is  
140 calculated relative to the background concentration without influence from this region such that:

$$141 \quad \text{observed } \Delta\text{CO}_2 = \text{observed } [\text{CO}_2] - \text{background } [\text{CO}_2] \quad (1)$$

142 following previous work (Sweeney et al., 2016; Commane et al., 2017; Jeong et al., 2018).

143 The background CO<sub>2</sub> concentrations at the NOAA BRW tower are determined by smoothing the 10-day mean of the  
144 observed ocean sector concentrations using spline fitting to produce a daily CO<sub>2</sub> background concentration. We calculate the  
145 uncertainty of these background concentrations by both 1) varying the starting hour of the 10-day mean calculation prior to  
146 spline fitting and 2) randomly sub-selecting 50% the ocean sector concentrations 1000 times. The interval that contains 95%  
147 of these 240,000 fits represents our daily background uncertainty. Figure S2 shows the ocean sector concentrations, resulting  
148 background concentration, and uncertainty described here.

149 To determine the background CO<sub>2</sub> concentrations for the ARM-ACME V and ABoVE Arctic-CAP aircraft  
150 campaigns, we isolate aircraft observations without surface influence from the North Slope using the WRF-STILT footprints  
151 as done for larger regions in Chang et al. (2014) and Commane et al. (2017). These observed CO<sub>2</sub> concentrations represent the  
152 state of the air before it interacts with the surface in the study region. The regional backgrounds vary by the direction from  
153 which the air enters the domain. For example, the backgrounds from the south and from over land generally experience CO<sub>2</sub>  
154 drawdown prior to those from over the Arctic Ocean. The time- and directional-dependent backgrounds we use are shown in



155 Fig. S3. We apply the uncertainty from the NOAA BRW tower background to the aircraft backgrounds as a reasonable  
156 representation of the variability associated with available background CO<sub>2</sub> concentration data.

### 157 2.3 Simulated atmospheric CO<sub>2</sub> concentration enhancement calculation

158 To understand how landscape interactions with the atmosphere (through CO<sub>2</sub> flux) influenced the observed CO<sub>2</sub> concentrations  
159 across space and time, we calculate the corresponding simulated ΔCO<sub>2</sub> [units: ppm] by transporting *bottom-up* biogenic CO<sub>2</sub>  
160 fluxes to each observation site such that:

$$161 \quad \text{simulated } \Delta\text{CO}_2 = \text{simulated CO}_2 \text{ flux} \times \text{simulated footprint} \quad (2)$$

162 In this calculation, we multiply the hourly simulated CO<sub>2</sub> flux [ $\mu\text{mol CO}_2 \text{ m}^{-2} \text{ s}^{-1}$ ] by the footprint [ppm ( $\mu\text{mol CO}_2 \text{ m}^{-2} \text{ s}^{-1}$ )<sup>-1</sup>]  
163 for that hour starting at the observation point, backward in time for each hour up to ten days, where the footprint quantifies  
164 the influence of the land surface on the concentration observed at a measurement point. The simulated ΔCO<sub>2</sub> is then the sum  
165 of these hours.

166 We use expected CO<sub>2</sub> fluxes based on a variety of bottom-up model approaches which represent North Slope  
167 ecosystems. Year-round bottom-up estimates of net CO<sub>2</sub> fluxes (defined by the models as net ecosystem exchange, NEE) are  
168 obtained from the Tundra Vegetation Photosynthesis and Respiration Model (TVPRM) ensemble, and from existing model  
169 output from Luus et al. (2017) and Commane et al. (2017). Independent bottom-up estimates of belowground CO<sub>2</sub> emissions  
170 (= NEE) for the cold season (net CO<sub>2</sub> uptake = 0) were obtained from Natali & Watts et al. (2019) and Watts et al. (2021). The  
171 TVPRM model ensemble development process is described in Sect. 2.4, and the other CO<sub>2</sub> flux models, including their native  
172 spatial and temporal resolutions, are listed in Table S2.

173 The footprints are calculated from the Lagrangian atmospheric transport modeling system, WRF-STILT (Stochastic  
174 Time-Inverted Lagrangian Transport model driven by Weather Research and Forecasting model meteorology (Henderson et  
175 al., 2015)). In this system, WRF meteorological fields are first generated for the study region and time period (v3.5.1 for ARM-  
176 ACME V and NOAA BRW tower footprints used here, v3.9.1 for ABoVE Arctic-CAP footprints). STILT then uses the WRF  
177 meteorology to estimate the contribution of surface fluxes to the atmospheric concentration at a specified time and place, called  
178 a receptor, by calculating the amount of time air (represented by a distribution of particles) spends in the lower half of the  
179 boundary layer at a given location. For this study, we use receptors set to correspond with the tower and aircraft CO<sub>2</sub>  
180 concentration observations. The footprints (and their corresponding measurements) for these receptors sample air from  
181 throughout the North Slope but are concentrated more heavily toward the area around the NOAA BRW tower (Fig. 1c).

182 For calculating simulated ΔCO<sub>2</sub> from the TVPRM ensemble, we grid the distribution of WRF-STILT particles and  
183 their corresponding surface influence to the spatial resolution of the meteorological reanalysis products driving the model. The  
184 CO<sub>2</sub> flux models used for comparison to the TVPRM ensemble are similarly treated using 0.5°-gridded 10-day WRF-STILT  
185 footprints, which are available on a circumpolar grid poleward of 30°N. The simulated CO<sub>2</sub> fluxes from Luus et al. (2017),  
186 Natali & Watts et al. (2019), and Watts et al. (2021) are regridded to 0.5° spatial resolution. For the models by Natali & Watts  
187 et al. (2019) and Watts et al. (2021), which only estimate monthly CO<sub>2</sub> fluxes, we apply a constant flux for that month. Since



188 the ends of our defined cold season (September–April) include transitional periods when some biogenic plant activity does  
189 occur (hence belowground CO<sub>2</sub> emissions ≠ NEE), for the Natali & Watts et al. (2019) and Watts et al. (2021) bottom-up  
190 scenarios, we add in estimates of photosynthesis and plant respiration fluxes from the TVPRM ensemble for April and  
191 September.

## 192 2.4 Empirically simulated biogenic CO<sub>2</sub> fluxes from tundra ecosystems

193 We develop the TVPRM as an ensemble of ecosystem-resolved models that represent a more extensive range of potential  
194 tundra ecosystem functional relationships, environmental drivers, and scaling assumptions than available from other CO<sub>2</sub> flux  
195 models. For this study, TVPRM generates a set of spatially and temporally varying CO<sub>2</sub> flux maps for a six-year period (2012–  
196 2017) at 30 × 30 km spatial and 1 hr temporal resolution for the Alaska North Slope.

197 TVPRM is driven by parameterized functional relationships for soil respiration (R<sub>soil</sub>), plant respiration (R<sub>plant</sub>), and  
198 photosynthesis (gross primary productivity (GPP)), which are described by:

$$199 \quad R_{\text{soil}} = \alpha_s \times T_s + \beta_s \quad (3)$$

$$200 \quad R_{\text{plant}} = \alpha_a \times T_a + \beta_a \quad (4)$$

$$201 \quad GPP = \lambda \times T_{\text{scale}} \times \text{SIF} \times \text{PAR} \times \frac{1}{1 + \frac{\text{PAR}}{\text{PAR}_0}} \quad (5)$$

$$202 \quad T_{\text{scale}} = \frac{(T_a - T_{\text{min}})(T_a - T_{\text{max}})}{(T_a - T_{\text{min}})(T_a - T_{\text{max}}) - (T_a - T_{\text{opt}})^2} \quad (6)$$

203 The simulated hourly CO<sub>2</sub> fluxes [units: μmol CO<sub>2</sub> m<sup>-2</sup> s<sup>-1</sup>] are determined as responses to light and heat: R<sub>soil</sub> is a function of  
204 near-surface soil temperature (T<sub>s</sub>) [°C]; R<sub>plant</sub> is a function of air temperature (T<sub>a</sub>) [°C]; and GPP is a function of a temperature  
205 scalar (T<sub>scale</sub>) and photosynthetically active radiation (PAR) [μmol photon m<sup>-2</sup> s<sup>-1</sup>], with solar-induced chlorophyll fluorescence  
206 (SIF) [mW m<sup>-2</sup> nm<sup>-1</sup> sr<sup>-1</sup>] used to define the seasonal cycle of photosynthetic capacity. T<sub>s</sub> depths are determined by reanalysis  
207 product and listed in Table S3. T<sub>scale</sub> ranges from 0 to 1 based on the position of T<sub>a</sub> on the continuum between minimum  
208 temperature (T<sub>min</sub> = 0°C), maximum temperature (T<sub>max</sub> = 40°C), and optimal temperature (T<sub>opt</sub> = 15°C). NEE is then calculated  
209 as:

$$210 \quad NEE = R_{\text{soil}} + R_{\text{plant}} - GPP \quad (7)$$

211 with positive NEE values indicating a net source of CO<sub>2</sub> into the atmosphere and negative NEE values meaning net movement  
212 of CO<sub>2</sub> into the biosphere. We use NEE to be synonymous with net CO<sub>2</sub> flux. Using SIF, which correlates to photosynthetic  
213 activity (Porcar-Castell et al., 2014; Yang et al., 2015), in the modeling framework provides an advantage over indices such  
214 as enhanced vegetation index (EVI) due to the limited canopy and evergreen nature of tundra ecosystems (Luus et al., 2017).

215 The parameter values (α<sub>s</sub>, β<sub>s</sub>, α<sub>a</sub>, β<sub>a</sub>, λ, PAR<sub>0</sub>) for the site-level relationships used by TVPRM are determined first  
216 using the observed net CO<sub>2</sub> fluxes from the eddy flux sites (see Sect. S1 in Supplement). We determine the site-level parameters  
217 separately for each combination of reanalysis product (NARR (Mesinger et al., 2006) and ERA5 (Hersbach et al., 2020)),  
218 which provide T<sub>a</sub>, T<sub>s</sub>, and PAR, and SIF product (GOME-2 (Joiner et al., 2016), GOSIF (Li and Xiao, 2019), and CSIF (Zhang



219 et al., 2018)) that will later be used to generate the regional TPVRM ensemble (Tables S3–S4, see Sects. S2–S3). Additional  
220  $\alpha_s$  and  $\beta_s$  parameters are determined using  $T_s$  from the Remote Sensing driven Permafrost Model (RS-PM (Yi et al., 2019,  
221 2018)) to test its implementation in TPVRM. RS-PM includes drivers and processes such as soil moisture and snow cover that  
222 more explicitly control the  $T_s$  throughout the soil column which better represent the zero-curtain period than the reanalysis  
223 products.

224 Using the median parameter values for each site, we simulate the TVPRM net CO<sub>2</sub> flux for our study period at every  
225 site location (Fig. S1). These simulated net CO<sub>2</sub> fluxes perform well against the net CO<sub>2</sub> flux observations at their  
226 corresponding sites (Figs. 1d, S4, see Sect. S4). This process also identifies two distinct ecosystem groups: “inland”,  
227 predominately graminoid and shrub tundra (ICS, ICT, ICH, IVO), and “coastal”, predominately wetland tundra (ATQ, BES,  
228 BEO, CMDL), based on the similar simulated CO<sub>2</sub> flux responses to the meteorology- and SIF-determined functional  
229 relationships within each group.

230 The net CO<sub>2</sub> flux for each meteorological grid box in our study domain is then calculated using the site-level  
231 functional relationships for both tundra groups. These fluxes are weighted by the spatial distribution of inland and coastal  
232 tundra from three different vegetation maps (CAVM (Walker et al., 2005), RasterCAVM (Raynolds et al., 2019), and ABoVE  
233 LC (Wang et al., 2020), Fig. S5, Table S5, see Sect. S5) to produce the regionally scaled TVPRM net CO<sub>2</sub> flux. By varying  
234 the choice of representative inland and coastal tundra sites, meteorological reanalysis product, vegetation map, and SIF  
235 product, we generate 288 different simulations (members) of net CO<sub>2</sub> flux (referred to here as the unconstrained TVPRM  
236 ensemble) for each grid box across the region for each of the six study years. Monthly and annual regional net CO<sub>2</sub> flux values  
237 are calculated as the area-weighted sum of all grid boxes simulated in our domain. Notable changes since the previous iteration  
238 of this empirical CO<sub>2</sub> flux model (Commane et al., 2017; Luus et al., 2017) include the expansion of the model to include  
239 multiple ensemble members to account for variability and uncertainty in model formulation, the use of additional site-years of  
240 CO<sub>2</sub> flux observations (with increased data coverage over the cold season), more inclusive data filtering methods, and much  
241 higher temporal (1-, 4-, and 8-day rather than monthly) and spatial (0.01° and 0.05° rather than 0.5°) resolution SIF datasets.  
242 We compare TVPRM to the previous model version by Luus et al. (2017) and its CARVE-informed optimization by Commane  
243 et al. (2017) in Sect. 3.3.

## 244 2.5 Evaluation Framework

245 We use the atmospheric CO<sub>2</sub> concentration observations to evaluate the many tundra ecosystem parameterizations, vegetation  
246 distributions, and environmental drivers that represent the net CO<sub>2</sub> flux on the North Slope over various spatial and temporal  
247 scales. For this assessment, we compare the observed  $\Delta\text{CO}_2$ , which are the observed CO<sub>2</sub> concentration changes driven by  
248 regional CO<sub>2</sub> fluxes, with the simulated  $\Delta\text{CO}_2$  determined by combining the regional biogenic CO<sub>2</sub> flux models with the  
249 atmospheric transport model.

250 To compare the regional observed  $\Delta\text{CO}_2$  and simulated  $\Delta\text{CO}_2$ , we calculated the coefficient of determination ( $R^2$ ) as  
251 the square of the Pearson correlation coefficient for all points. The slope ( $m$ ) is determined by ordinary least squares using the





252 median of each 10% bin of ordered observed and corresponding simulated net CO<sub>2</sub> flux. The normalized mean bias (NMB) of  
253 all points is defined as  $\frac{\sum(\text{simulated} - \text{observed})}{\sum \text{observed}}$ . The root-mean-square error (RMSE) of all points is defined as

254  $\sqrt{(\text{simulated} - \text{observed})^2}$ .

255 These comparisons enable us to constrain the regional net CO<sub>2</sub> flux on the Alaska North Slope. First, we identify the  
256 year-round empirically driven net CO<sub>2</sub> fluxes from the TVPRM ensemble which are most consistent with the CO<sub>2</sub>  
257 concentration observations from the two aircraft campaigns and at the tower. Then, noting the large range in potential cold  
258 season CO<sub>2</sub> fluxes, we compare our constrained TVPRM member with CO<sub>2</sub> fluxes from previous studies. Finally, we suggest  
259 and quantify sources of the missing CO<sub>2</sub> flux observed during the early cold season (defined here as September–December)  
260 and incorporate those fluxes into our net CO<sub>2</sub> budget. This analysis provides a unique regional net CO<sub>2</sub> flux quantification for  
261 the North Slope that is verified using atmospheric observations and can also be explained from an ecological and physical  
262 perspective.

### 263 3. Results

#### 264 3.1 Evaluation of unconstrained empirical net CO<sub>2</sub> flux model ensemble

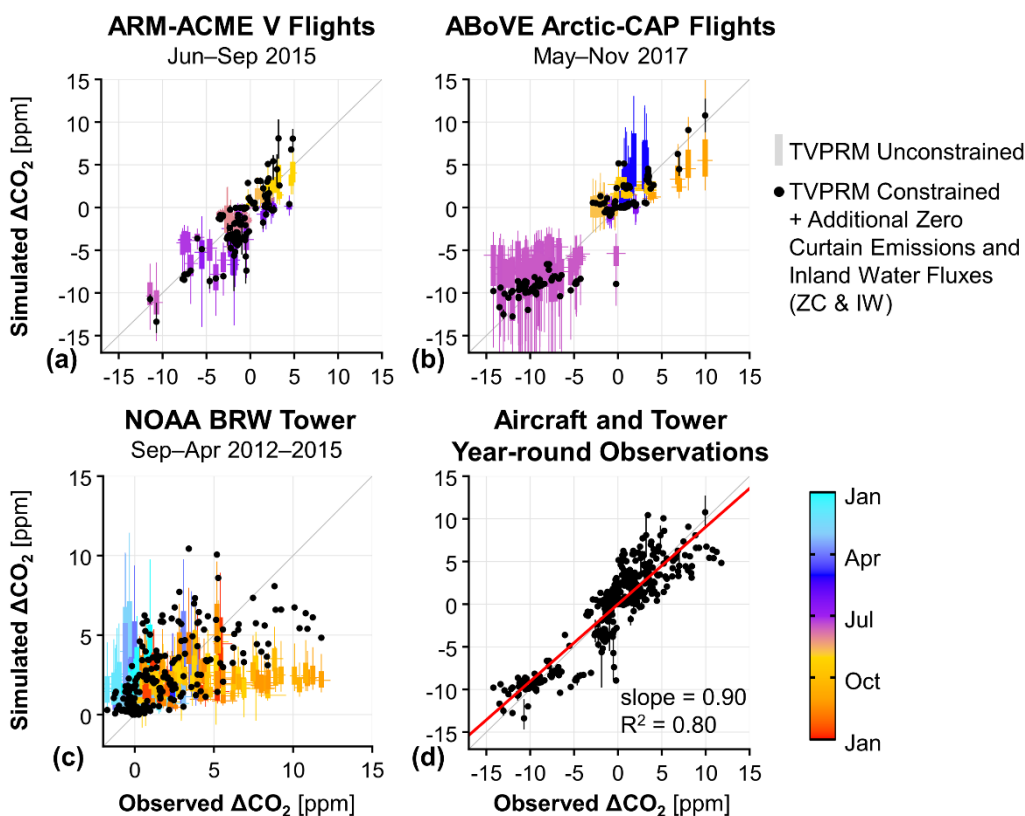
##### 265 3.1.1 Using aircraft-observed CO<sub>2</sub> enhancements

266 The observed ΔCO<sub>2</sub> during the ARM-ACME V (June–September 2015) and ABoVE Arctic-CAP (May–November 2017)  
267 airborne campaigns show a strong seasonal uptake pattern throughout the growing season (Figs. 2a–2b). The frequent flights  
268 during ARM-ACME V (multiple flights per week) observe the transition from early to peak growing season uptake (observed  
269 ΔCO<sub>2</sub> = –11 ppm) and on into cold season respiration, which results in net CO<sub>2</sub> source conditions in September (+5 ppm).  
270 While less frequent, the ABoVE Arctic-CAP flights begin at the end of the cold season, extend later into following cold season,  
271 and cover a larger area of the North Slope. Peak growing season uptake observed by the ABoVE Arctic-CAP flights (–14 ppm)  
272 is slightly stronger than for during ARM-ACME V, and by November, the ABoVE Arctic-CAP flights observe a strong CO<sub>2</sub>  
273 source throughout the North Slope (+10 ppm). The difference in observed ΔCO<sub>2</sub> during peak growing season uptake between  
274 2015 and 2017 is likely similar to the uncertainty in the respective values and could be due to differences in areas of the North  
275 Slope sampled between years.

276 The magnitude and timing of the observed net CO<sub>2</sub> uptake throughout the growing season is generally well  
277 represented by the empirical net CO<sub>2</sub> flux model ensemble (TVPRM Unconstrained, Figs. 2a–2b, S6). The median coefficients  
278 of determination (R<sup>2</sup>) and ordinary least squares slopes between the observed and simulated ΔCO<sub>2</sub> for this time are 0.54 and  
279 0.41 for ARM-ACME V and 0.82 and 0.72 for ABoVE Arctic-CAP, respectively. Only for the July observations during the  
280 ABoVE Arctic-CAP campaign do many members of the CO<sub>2</sub> flux trend toward an underestimate of net CO<sub>2</sub> uptake, with all  
281 points showing a much larger range in simulated values compared to ARM-ACME V. The net CO<sub>2</sub> release tends to be



282 overestimated by the TVPRM ensemble during the ABoVE Arctic-CAP seasonal transitions in May and September, but during  
283 November the observed soil respiration is consistently underestimated.



284  
285 **Figure 2.** Aircraft and tower CO<sub>2</sub> concentration measurements constrain year-round simulated CO<sub>2</sub> fluxes on the Alaska North Slope. (a)–  
286 (c) Comparison of observed and simulated ΔCO<sub>2</sub> during the ARM-ACME V flight campaign (a), during the ABoVE Arctic-CAP flight  
287 campaign (b), and at the NOAA BRW tower (c) for air over the Alaska North Slope. Horizontal lines indicate range of uncertainty in the  
288 NOAA BRW tower ocean sector background calculation. Vertical boxes represent 50% and whiskers represent 95% of ΔCO<sub>2</sub> values from  
289 all members of unconstrained TVPRM ensemble (see Sect. 2.4) from all binned points and are colored by month of year. For (a)–(b),  
290 observed values are vertically binned medians, and for constrained TVPRM member + additional zero-curtain emissions (ZC) and inland  
291 water fluxes (IW), vertical lines contain middle 95% of ΔCO<sub>2</sub> values from all binned points. (d) Combined comparison of observed and  
292 simulated ΔCO<sub>2</sub> for all aircraft and tower points using constrained TVPRM member + ZC & IW. Shown with linear best fit (red line), slope  
293 determined by ordinary least squares, and coefficient of determination (R<sup>2</sup>) of all points (n = 455). 1:1 line shown in dark grey.

294 Given the large range of unconstrained representations of the regional CO<sub>2</sub> flux, the accuracy in simulating the aircraft  
295 observed ΔCO<sub>2</sub> varies between TVPRM ensemble members. For example, members using the RasterCAVM vegetation map,  
296 which places less coastal tundra area cover in the south (Fig. S5), produce a smaller mean July net CO<sub>2</sub> uptake flux (by ~1  
297 μmol m<sup>-2</sup> s<sup>-1</sup>, Fig. S7a) throughout the southern North Slope than members using other vegetation maps (CAVM and ABoVE  
298 LC), and this placement consistently underestimates the net ΔCO<sub>2</sub> uptake during the growing season compared to the aircraft  
299 observations by 5–10 ppm (Fig. S8). Also, members driven by SIF products that integrate additional remote sensing and/or  
300 meteorological data (GOSIF and CSIF) better reflect the timing and magnitude of the peak season carbon uptake in tundra



301 ecosystems than members produced by interpolated SIF retrievals (GOME-2 SIF product), which underestimate the observed  
302 CO<sub>2</sub> uptake during July (Fig. S8).

303 Using these comparisons, we identify less-representative ensemble members that generally underestimate the  
304 observed ΔCO<sub>2</sub> uptake during the growing season (RasterCAVM vegetation map and GOME-2 SIF product members).  
305 Removing these members from the TVPRM ensemble improves the collective performance of the remaining members during  
306 the growing season (Fig. S6), brings the median slope of agreement closer to 1 for both campaigns (improves from 0.53 to  
307 0.64 and from 0.71 to 0.94 for ARM-ACME V and ABoVE Arctic-CAP, respectively), and reduces median NMB (−0.34 to −  
308 0.03) and median RMSE (3.12 to 2.73) for ABoVE Arctic-CAP.

### 309 3.1.2 Using tower-observed CO<sub>2</sub> enhancements

310 As seen with the September–November aircraft data, the observed ΔCO<sub>2</sub> at the NOAA BRW tower (Fig. 2c) indicate that the  
311 CO<sub>2</sub> source to the atmosphere increases substantially from September to peak in October and November (+12 ppm) before  
312 decreasing to near zero throughout the late cold season (January–April).

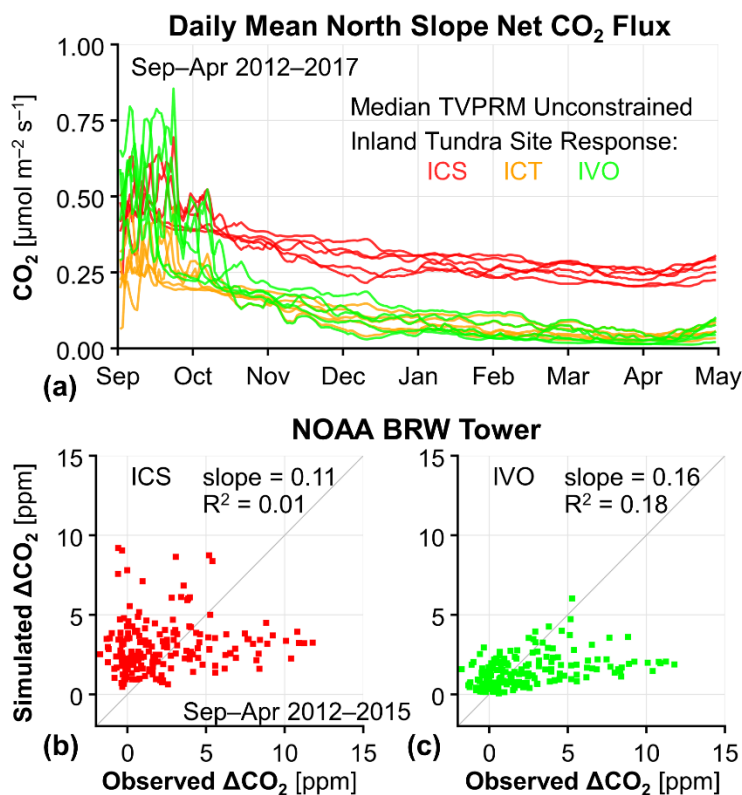
313 Most of the TVPRM ensemble members substantially underestimate the observed ΔCO<sub>2</sub> in the early cold season  
314 (September–December) as the soils freeze, and some simulations produce too much CO<sub>2</sub> in the late cold season when the soils  
315 are frozen (Fig. 2c). The cold season CO<sub>2</sub> flux differs greatest in magnitude and spatial extent between the ensemble members  
316 parameterized for the ICS and ICT inland tundra sites (Figs. 3a, S9–S10), with a net CO<sub>2</sub> flux difference of ~0.2 μmol m<sup>−2</sup> s<sup>−1</sup>  
317 throughout the region (Fig. S7b).

318 While the magnitude of CO<sub>2</sub> flux from ICS members better matches the observed ΔCO<sub>2</sub> in the early cold season than  
319 from other sites (Figs. 3b, S11), the response to soil temperature at ICS shows only a modest decrease in CO<sub>2</sub> flux between the  
320 early and late cold season (Fig. 3a, 32% decrease between October and March), resulting in an overestimate of the regional  
321 ΔCO<sub>2</sub> in the late cold season. The CO<sub>2</sub> flux response to soil temperature for ICT members is similar to that for ICS but lower  
322 in magnitude, and the simulated ΔCO<sub>2</sub> from members of neither site performs well against the observations in both the early  
323 and late cold season. Therefore, ICS and ICT inland tundra responses to soil temperature are not representative of the regional  
324 ΔCO<sub>2</sub> observed at the NOAA BRW tower throughout the entire cold season, and we remove those members from our TPVRM  
325 ensemble.

326 The observed net CO<sub>2</sub> fluxes at the IVO inland tundra and CMDL coastal tundra sites both show prolonged zero-  
327 curtain emissions (Fig. S1) and respond strongly to soil temperature in the early cold season (Fig. S9). The stronger response  
328 of CO<sub>2</sub> fluxes to soil temperature from the early to late cold season at IVO (Fig. 3a, 70% decrease by January) compared to at  
329 the Imnavait Creek sites produces TVPRM members that better represents the large regional decrease in ΔCO<sub>2</sub> observed on  
330 the North Slope (Fig. 3c). While all coastal tundra sites respond similarly to soil temperature during the cold season, we  
331 determine that the CO<sub>2</sub> flux magnitude at CMDL is most consistent with the regional observations (Fig. S11). Soil temperatures  
332 from ERA5 remain warmer throughout the late cold season compared to those from NARR, which causes simulations using

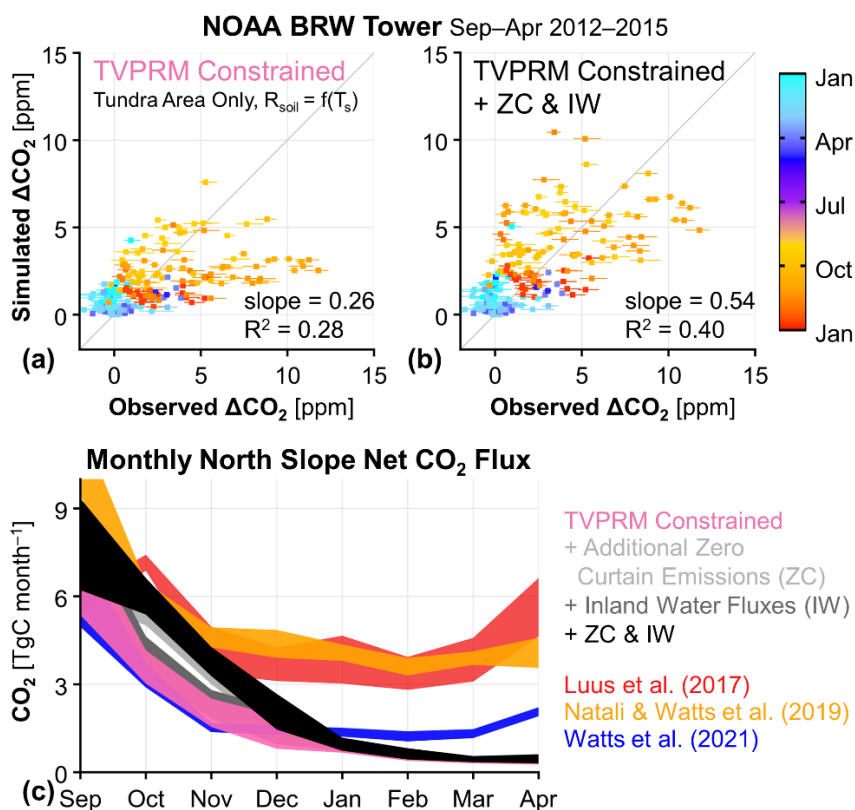


333 ERA5 soil temperatures to overestimate CO<sub>2</sub> release during that time (Fig. S11). Unlike during the growing season, cold season  
334 CO<sub>2</sub> fluxes are not sensitive to the vegetation distribution and SIF products.



335  
336 **Figure 3.** Cold season CO<sub>2</sub> emissions for inland tundra site parameterizations and comparison to tower observations. (a) Timeseries of  
337 simulated daily mean Alaska North Slope net CO<sub>2</sub> flux for the median of all unconstrained TVPRM ensemble members using each of three  
338 inland tundra site parameterizations: ICS (red), ICT (orange), and IVO (green). Yearly colored lines shown for Sep–Apr beginning in Sep  
339 2012 and ending in Apr 2017. Same for all eight eddy flux sites shown in Fig. S9. (b)–(c) Comparison of observed and simulated ΔCO<sub>2</sub> at  
340 the NOAA BRW tower for air over the North Slope using the median of all unconstrained TVPRM ensemble members for the inland tundra  
341 site parameterizations at ICS (b, red) and IVO (c, green). Shown with slope determined by ordinary least squares and coefficient of  
342 determination (R<sup>2</sup>) of all points (n = 191). 1:1 line shown in dark gray.

343 Finally, we identify the TVPRM member that best matches the observed ΔCO<sub>2</sub>: parameterized by IVO inland tundra  
344 and CMDL coastal tundra site responses, distributed by the ABoVE LC vegetation map, and driven by NARR reanalysis and  
345 the CSIF SIF product (referred to here as TVPRM Constrained, Figs. S6, S12). This constrained simulation estimates a mean  
346 regional CO<sub>2</sub> flux of 0.05 μmol m<sup>-2</sup> s<sup>-1</sup> for the late cold season in 2012–2015 and reproduces well the observed ΔCO<sub>2</sub> during  
347 this time (Fig. 4a). The late cold season NMB and RMSE against the observations at the NOAA BRW tower are reduced from  
348 4.91 to 2.04 and from 1.94 to 1.30, respectively, for the constrained simulation compared to the median of the entire TVPRM  
349 ensemble (Fig. S12). However, the early cold season CO<sub>2</sub> emissions, with a mean regional CO<sub>2</sub> flux of 0.25 μmol m<sup>-2</sup> s<sup>-1</sup> for  
350 September–December (Fig. S13a), are still underestimated, with the simulated ΔCO<sub>2</sub> lower than the observed ΔCO<sub>2</sub> by ~5  
351 ppm (Fig. 4a).



352

353 **Figure 4.** Tall tower atmospheric observations of the Alaska North Slope support early cold season emissions not driven by soil temperature  
 354 and present no evidence for elevated late cold season emissions. **(a)–(b)** Comparison of hourly cold season (Sep–Apr) observed and simulated  
 355  $\Delta\text{CO}_2$  at the NOAA BRW tower for the constrained TPVRM member, where soil respiration ( $R_{\text{soil}}$ ) is determined only by soil temperature  
 356 ( $T_s$ ) **(a)** and for the constrained TVPRM member + additional zero-curtain emissions (ZC) and inland water fluxes (IW) **(b)**. Horizontal  
 357 segments indicate range of uncertainty in the NOAA BRW tower ocean sector background calculation. Shown with slope determined by  
 358 ordinary least squares and coefficient of determination ( $R^2$ ) of all points ( $n = 191$ ). 1:1 line shown in dark gray. **(c)** Monthly cold season total  
 359 Alaska North Slope net  $\text{CO}_2$  fluxes for various  $\text{CO}_2$  flux models. TVPRM-based simulations and Natali & Watts et al. (2019) show values  
 360 for 2012–2017, Luus et al. (2017) show 2012–2014, and Watts et al. (2021) show Sep 2016–Apr 2017. Ribbons represent range of all years,  
 361 where applicable. Area of the North Slope domain used to calculate regional totals is  $3.537 \times 10^5 \text{ km}^2$ .

### 362 3.2 Alternative soil temperature products and soil respiration parameterizations

363 To test the impact of reanalysis soil temperature on the early cold season  $\text{CO}_2$  fluxes, we implement soil temperatures that  
 364 better account for the controls of more complex tundra permafrost freeze-thaw processes like soil moisture and snow cover  
 365 than the reanalysis products driving our constrained TPVRM member. A single layer of soil temperature at 8 cm depth from  
 366 RS-PM captures the magnitude and temporal behavior of the observed early cold season  $\text{CO}_2$  fluxes slightly better than the  
 367 constrained member, which uses NARR reanalysis soil temperature and does not incorporate permafrost-model derived soil  
 368 temperature (Fig. S14a). The RS-PM soil temperature extends  $\text{CO}_2$  emission fluxes further into the cold season by up to a  
 369 month, which is consistent with a better representation of the zero-curtain period, however, emissions remain higher throughout



370 the late cold season than our atmospheric observation-constrained CO<sub>2</sub> fluxes (Fig. S15). We also test the implementation of  
371 a multi-layer fit driven by soil column temperature from RS-PM, but neither of these instances of remote sensing informed  
372 soil temperatures substantially improve the agreement of the ΔCO<sub>2</sub> at the NOAA BRW tower during the early cold season.  
373 Attempts to use alternative respiration formulations based on soil temperature, including Q<sub>10</sub> relationships, also fail to  
374 reproduce the observed elevated CO<sub>2</sub> fluxes during the cold season.

### 375 **3.3 Evaluation of other CO<sub>2</sub> flux models during the cold season**

376 More early cold season (September–December) CO<sub>2</sub> flux into the atmosphere is observed at the NOAA BRW tower than is  
377 emitted by our constrained empirical simulation member, and these observations also indicate low late cold season (January–  
378 April) CO<sub>2</sub> emissions. We compare our constrained CO<sub>2</sub> fluxes to several other representations of gridded CO<sub>2</sub> flux on the  
379 North Slope (Table S2) and find that difficulty in simulating the magnitude and timing of the observed ΔCO<sub>2</sub> throughout the  
380 cold season is not unique to the constrained fluxes from our study.

381 The net CO<sub>2</sub> fluxes from Luus et al. (2017) are similar to the constrained TVPRM member during the growing season  
382 (Fig. S16), but release more than three times as much CO<sub>2</sub> into the atmosphere throughout the late cold season (Fig. 4c). This  
383 large late cold season CO<sub>2</sub> flux leads to a large overestimate compared to the observed ΔCO<sub>2</sub> (Fig. S14b). The optimization  
384 employed by Commane et al. (2017) increases the September–October CO<sub>2</sub> flux to a range that matches our observations at  
385 the NOAA BRW tower. However, Commane et al. (2017) did not optimize the cold season fluxes from November to March,  
386 but reverted to Luus et al. (2017) fluxes during this time, thus producing late cold season fluxes that are too large. Overall,  
387 Commane et al. (2017) projected a regional total cold season CO<sub>2</sub> source of 37–40 TgC for 2012–2014, which is more than  
388 twice as high as our constrained TVPRM member CO<sub>2</sub> flux (15–18 TgC) for those years.

389 Carbon dioxide fluxes from work by Natali & Watts et al. (2019), a cold season model developed for the global high  
390 latitude permafrost region, are similar to our constrained TVPRM member in September, but the fluxes remain high throughout  
391 the cold season (Fig. 4c) similarly to Luus et al. (2017), for a range of total cold season CO<sub>2</sub> flux of 40–43 TgC for 2012–  
392 2017. This sustained CO<sub>2</sub> release also leads to an overestimation in the ΔCO<sub>2</sub> in the late cold season for this region (Fig. S14c).  
393 Tao et al. (2021) also show that the cold season CO<sub>2</sub> fluxes of Natali & Watts et al. (2019) are high compared to their model.  
394 More recent work by Watts et al. (2021), using observations from new Soil Respiration Station monitoring sites in Alaska,  
395 produces cold season CO<sub>2</sub> fluxes more similar to our constrained CO<sub>2</sub> fluxes, with an underestimate in the simulated ΔCO<sub>2</sub>  
396 during the early cold season (Fig. S14d), for a total cold season CO<sub>2</sub> flux of 18 TgC for September 2016 to April 2017.

### 397 **3.4 Sources of missing CO<sub>2</sub> fluxes**

398 None of the flux products discussed above, including our TVPRM ensemble, account for potential CO<sub>2</sub> fluxes during the zero-  
399 curtain not driven by soil temperature or from areas on the terrestrial-aquatic interface. To account for these processes, we first  
400 add an additional CO<sub>2</sub> flux with zero-curtain timing to our constrained CO<sub>2</sub> flux (TVPRM) member from both inland and  
401 coastal tundra areas that consists of 0.25 μmol m<sup>-2</sup> s<sup>-1</sup> for October with a reduction to zero by the end of December. This



402 additional CO<sub>2</sub> flux is within the daily variability of the observed CO<sub>2</sub> flux at the IVO and CMDL eddy flux sites during the  
403 zero-curtain period (Fig. S9) and improves the ability to reproduce the observed ΔCO<sub>2</sub> at the NOAA BRW tower (slope =  
404 0.46, R<sup>2</sup> = 0.41). We also apply the coastal tundra site ecosystem parameterization used in our constrained TVPRM member  
405 to all areas of inland water on the North Slope, which account for 4% of the domain and were previously set to zero CO<sub>2</sub> flux  
406 (Fig. S5). Representing these aquatic areas with biogenic CO<sub>2</sub> fluxes consistent with coastal tundra ecosystems is one way to  
407 bridge the terrestrial-aquatic gap in tundra ecosystem models and improves the performance of our model (slope = 0.32, R<sup>2</sup> =  
408 0.30 against NOAA BRW tower observations). The magnitude of additional zero-curtain flux suggested here and the portion  
409 of inland water represented with coastal tundra site parameterizations produce the best statistical comparison for a range of  
410 choices tested (Fig. S17).

411 Together, adding these zero-curtain (ZC) and inland water (IW) CO<sub>2</sub> fluxes to our constrained simulation (referred to  
412 as TVPRM Constrained + ZC & IW) increases the mean regional CO<sub>2</sub> flux in early cold season by 70% (0.18 μmol m<sup>-2</sup> s<sup>-1</sup>,  
413 Fig. S13b) and results in a large improvement to our comparison of ΔCO<sub>2</sub> at the NOAA BRW tower (slope = 0.54, R<sup>2</sup> = 0.40,  
414 Figs. 4b, S12) and across the region using airborne data, especially during the November ABoVE Arctic-CAP flights (Figs. 2,  
415 S6). The year-round comparison using all available aircraft and tower observations shows these net CO<sub>2</sub> fluxes are now  
416 representative of the region (slope = 0.90, R<sup>2</sup> = 0.80, Fig. 2d). As a result, the North Slope regional total cold season CO<sub>2</sub> flux  
417 increases by 6 TgC (~38%) to 20–24 TgC for 2012–2017 compared to the constrained empirical CO<sub>2</sub> flux model member.

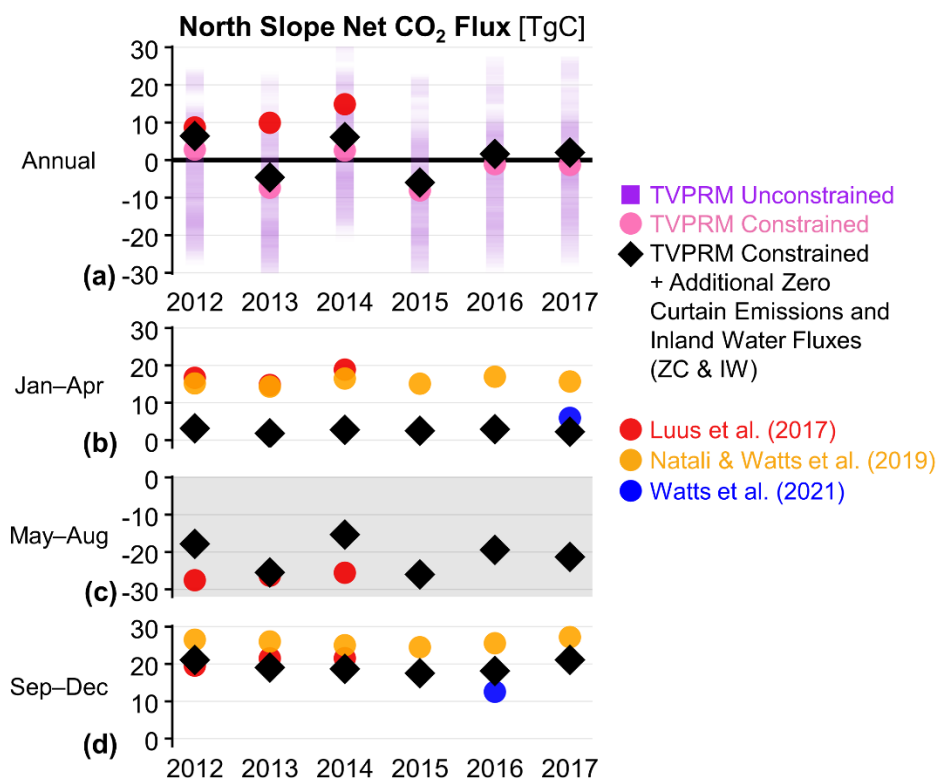
### 418 3.5 Alaska North Slope annual net CO<sub>2</sub> flux

419 The median Alaska North Slope annual net CO<sub>2</sub> flux from the TVPRM ensemble (–5 TgC yr<sup>-1</sup>) for 2012–2017 is consistent  
420 with the previous multi-model comparison (Fisher et al., 2014), but we find a much smaller range in regional CO<sub>2</sub> flux values  
421 (26 TgC yr<sup>-1</sup> to –29 TgC yr<sup>-1</sup> for 95% of TVPRM members) (Fig. S18). The largest contribution to this ensemble range comes  
422 from the difference in parameterizations determined for the ICS and ICT inland tundra sites, with TVPRM members using ICS  
423 trending toward a net CO<sub>2</sub> source, while ICT trends toward net CO<sub>2</sub> uptake. The distribution of inland and coastal tundra  
424 throughout the region represented by the vegetation maps also has a noticeable impact on the sign of the net CO<sub>2</sub> flux, with  
425 members using the RasterCAVM more likely to release net CO<sub>2</sub> into the atmosphere than members using the other maps.  
426 There is also little interannual variability in the unconstrained TVPRM ensemble, with only 2014 moving toward a net CO<sub>2</sub>  
427 source, consistent with Tao et al. (2021) for these years.

428 Our best quantification of the annual net CO<sub>2</sub> flux for the North Slope informed by atmospheric observations, TVPRM  
429 Constrained + ZC & IW, indicates that the region is a small net sink for 2013 (–5 TgC yr<sup>-1</sup>) and 2015 (–6 TgC yr<sup>-1</sup>) and a small  
430 net source for 2012 (+6 TgC yr<sup>-1</sup>), 2014 (+6 TgC yr<sup>-1</sup>), 2016 (+2 TgC yr<sup>-1</sup>), and 2017 (+2 TgC yr<sup>-1</sup>) (Fig. 5a). We estimate a  
431 10% uncertainty in the net annual CO<sub>2</sub> flux based on the slope from our final comparison with the year-round observations  
432 (Fig. 2d). The year-round net CO<sub>2</sub> fluxes from Luus et al. (2017) (driven with NARR meteorology, monthly GOME-2 SIF,  
433 and CAVM vegetation map) indicate the North Slope to be a strong annual net CO<sub>2</sub> source for 2012–2014 (+9 TgC yr<sup>-1</sup> to +15



434 TgC yr<sup>-1</sup>, Fig. S18) and are inconsistent with our results. Our results are more consistent with Tao et al. (2021), but we find a  
 435 smaller range in the magnitude of net CO<sub>2</sub> flux over the same years and more years trending toward a net CO<sub>2</sub> source.  
 436



437  
 438 **Figure 5.** Annual and seasonal Alaska North Slope net CO<sub>2</sub> flux constrained by aircraft and tower observations. (a) Annual, (b) late cold  
 439 season (Jan–Apr), (c) growing season (May–Aug), and (d) early cold season (Sep–Dec) total Alaska North Slope net CO<sub>2</sub> fluxes for various  
 440 CO<sub>2</sub> flux models for 2012–2017 as in Fig. 4. Purple squares indicate middle 95% of all TVPRM ensemble members.

441 We find that the regional net growing season CO<sub>2</sub> uptake and the cold season emissions on the North Slope are  
 442 comparable in magnitude, so the net balance could depend on small perturbations in either flux. However, the regional cold  
 443 season CO<sub>2</sub> emissions for these years were relatively similar from year to year: 18–21 TgC for the early cold season (Fig. 5d),  
 444 diminishing to only 2–3 TgC for the late cold season (Fig. 5b). Therefore, the interannual variability of the regional carbon  
 445 balance is largely driven by fluctuating net growing season CO<sub>2</sub> fluxes during these years: greater net growing season uptake  
 446 in 2013 and 2015 than in 2012, 2014, 2016, and 2017 (Fig. 5c).





#### 447 4. Discussion

##### 448 4.1 Tundra ecosystem growing season net CO<sub>2</sub> fluxes

449 The performance of the TVPRM ensemble against the atmospheric observations during the growing season indicates that the  
450 tundra ecosystems of the Alaska North Slope respond to light and heat as expected given previous knowledge, and that the net  
451 CO<sub>2</sub> flux is largely controlled by the simple  $R_{\text{soil}}$ ,  $R_{\text{plant}}$ , and GPP relationships in the empirical model over this time.

452 The regional net CO<sub>2</sub> flux is highly sensitive, however, to the distribution of tundra vegetation types (upland v.  
453 coastal) throughout the North Slope during the growing season. Since coastal tundra takes up more CO<sub>2</sub> for a given unit PAR  
454 compared to inland tundra, based on the relationships between observed site-level net CO<sub>2</sub> flux and PAR (TVPRM parameters),  
455 the fact that vegetation distributions with more coastal tundra to the south (CAVM (Walker et al., 2005), ABoVE LC (Wang  
456 et al., 2020)) better agree with the observations suggests the ecosystem response of the southern North Slope is consistent with  
457 coastal ecosystems. This result also supports the importance of accurate ecosystem type locations in upscaling eddy flux  
458 measurements and highlights the need for improved vegetation mapping and classification in the Arctic ecology research  
459 community.

460 The seasonal cycle of photosynthetic activity, represented in the TVPRM ensemble by SIF, also strongly impacts the  
461 growing season regional net CO<sub>2</sub> flux. Our study years with greater net CO<sub>2</sub> uptake correspond to growing seasons with  
462 stronger SIF signals, which is related to increased productivity, and consistent with previous studies (e.g., Magney et al., 2019;  
463 Sun et al., 2017). Although there is not a consistent correlation with increases in air temperature and PAR during these years,  
464 the larger uptake may be due to a combination of these and/or other drivers not accounted for explicitly in our empirical  
465 simulation that are represented by SIF.

##### 466 4.2 Regional-scale cold season CO<sub>2</sub> emissions

467 Observations across scales, at the in-situ eddy flux towers, the NOAA BRW tower, and from aircraft, consistently show  
468 signs of large early cold season CO<sub>2</sub> emissions from ecosystems on the Alaska North Slope. However, there is no evidence of  
469 widespread elevated emissions in this region during the late cold season, contrary to other studies (Commane et al., 2017;  
470 Natali & Watts et al., 2019). The TVPRM ensemble parameterizations using terrestrial eddy flux sites and the fluxes from  
471 other terrestrial CO<sub>2</sub> models cannot reproduce both the observed magnitude and across-season timing of these cold season CO<sub>2</sub>  
472 emissions.

473 The largest differences in the net CO<sub>2</sub> flux between TVPRM ensemble members result from the contrasting site conditions  
474 driving the ICS and ICT soil respiration parameterizations during the cold season. When taken separately by cold season  
475 segment, ICS members perform quite well against observations at the NOAA BRW tower for early cold season and ICT  
476 members perform well for the late cold season. The ecosystems sampled by the ICS tower are seasonally inundated and retain  
477 a deep layer of organic soil that can be respired in greater amounts longer into the early cold season, while the well-drained  
478 hillslope at ICT does not allow for accumulation of organic matter in the same way (Euskirchen et al., 2017; Larson et al.,



479 2021). The early-to-late cold season reduction in CO<sub>2</sub> fluxes at these sites is not consistent with the observed regional  
480 atmospheric trend, however, and we remove the members parameterized by them from the ensemble. While individual eddy  
481 flux site parameterizations may reproduce regional CO<sub>2</sub> fluxes for a given season, it is important to consider their response to  
482 drivers across multiple seasons when scaling from the site-level to regional domains.

483 The observed cold season CO<sub>2</sub> flux pattern on the North Slope may be unique to tundra ecosystems of this region. For  
484 example, the CO<sub>2</sub> fluxes from Natali & Watts et al. (2019) and Watts et al. (2021) both incorporate measurements from the  
485 North Slope. However, Natali & Watts et al. (2019) used boosted regression trees trained on belowground respiration  
486 measurements from across the pan-Arctic tundra and boreal zones, which may not be representative for our study region. The  
487 fluxes from Watts et al. (2021) are based on respiration measurements from throughout only Alaska and northwest Canada  
488 and conform better to local conditions. The evaluation of these CO<sub>2</sub> fluxes against atmospheric CO<sub>2</sub> measurements also  
489 produces results that are more consistent with our TVPRM ensemble determined by North Slope eddy flux tower  
490 measurements.

491 We find that the atmospheric observations are best matched by biogenic CO<sub>2</sub> fluxes that include an additional CO<sub>2</sub> source  
492 from tundra ecosystems during the zero-curtain period that are independent from soil temperature variability and year-round  
493 net CO<sub>2</sub> fluxes from areas of inland water. The additional zero-curtain flux represents large-scale emission events not directly  
494 related to microbial activity and root respiration controlled by soil temperature, but could be related to the physical release of  
495 CO<sub>2</sub> from soil through the snowpack as the soil layers remain unfrozen (Bowling and Massman, 2011). The Alaska North  
496 Slope also has many water bodies distributed throughout the coastal tundra region, and the extent to which carbon cycles  
497 between small, shallow ponds and their surrounding terrestrial components is unclear (Magnússon et al., 2020). The biogenic  
498 CO<sub>2</sub> fluxes in these areas are likely driven by ecosystem-scale CO<sub>2</sub> fluxes from both coastal tundra and small ponds (Holgerson  
499 and Raymond, 2016; Tan et al., 2017) and their impact on the regional net CO<sub>2</sub> flux, via both emissions and uptake, may be  
500 significant (Elder et al., 2018; Beckebanze et al., 2022). Only by adding fluxes that match observed zero-curtain CO<sub>2</sub> emission  
501 pulses and by approximating net CO<sub>2</sub> fluxes in aquatic areas can we reproduce the observed ΔCO<sub>2</sub> magnitude in both early  
502 and late cold season. The resulting seasonal change between the early and late cold season is consistent with the extended  
503 duration of the observed regional-scale zero curtain.

#### 504 **4.3 Future state of net CO<sub>2</sub> flux on the Alaska North Slope**

505 As the Arctic warms rapidly, the competition between the growing and cold season Arctic CO<sub>2</sub> fluxes will determine the net  
506 biogenic CO<sub>2</sub> flux into the atmosphere. Warming air temperature warms soils, thaws permafrost, increases active layer  
507 thickness and has extended the duration of the zero curtain from weeks to over 100 days (Romanovsky and Osterkamp, 2000;  
508 Schuur et al., 2015; Zona et al., 2016), all of which increase cold season CO<sub>2</sub> emissions. The warming may also increase net  
509 growing season uptake, but the severe light limitation at high northern latitudes limits the extent of the growing season,  
510 especially on the North Slope (Zhang et al., 2020). The future of CO<sub>2</sub> fluxes from inland waters and wetlands in the Arctic is  
511 uncertain, but some studies suggest CO<sub>2</sub> emissions from lakes may increase (Bayer et al., 2019). The culmination of these



512 effects will likely push the North Slope into a consistent net source in the future. However, observations at the NOAA BRW  
513 tower during our study period do not show elevated late cold season CO<sub>2</sub> emissions, so the North Slope was not a consistent  
514 net source through 2017. Accordingly, care must be taken to accurately represent CO<sub>2</sub> fluxes from Arctic ecosystems during  
515 both the early and late cold season when calculating the annual net CO<sub>2</sub> budget.

516 Our results motivate the need for a more extensive network of CO<sub>2</sub> eddy flux towers operating year-round, alongside  
517 sensors for soil moisture and soil temperature profiles throughout the active layer to better understand the mechanisms driving  
518 year-round and especially early cold season CO<sub>2</sub> fluxes. Noting that automated or semi-automated monitoring systems for  
519 aquatic environments currently do not exist for the North Slope or other high latitude regions, this sensor network should be  
520 distributed throughout poorly sampled ecosystem types, particularly along wetness gradients that span mixed terrestrial-aquatic  
521 environments. The results in this study also support the need for additional continuous CO<sub>2</sub> concentration measurements at tall  
522 towers across the North Slope (including away from the coast) to increase coverage of observed ΔCO<sub>2</sub> during all seasons and  
523 to better constrain the regional background. Airborne measurements of both CO<sub>2</sub> concentrations and CO<sub>2</sub> fluxes remain  
524 valuable to sample areas less accessible via ground-based measurements, but a large-scale flight campaign in the region has  
525 not occurred since 2017. Any additional flights should be targeted as early before, and as late after, the growing season as  
526 possible. While we can constrain the annual net CO<sub>2</sub> budget with existing data, the Arctic is rapidly changing and needs  
527 constant monitoring. These recommendations would provide more detailed spatial and seasonal constraints and up-to-date  
528 information on the processes driving CO<sub>2</sub> fluxes across the region.

## 529 **5. Conclusions**

530 Observed atmospheric concentrations from aircraft and towers are a powerful tool that provide a regional constraint on the  
531 many combinations of possible CO<sub>2</sub> flux parameterizations and distributions of tundra ecosystems on the North Slope of  
532 Alaska. We find that the annual regional net CO<sub>2</sub> flux on the North Slope is not a consistent net source or sink, but instead  
533 varies between -6 and +6 TgC yr<sup>-1</sup> for 2012–2017. We can also identify ecosystem relationships and driver combinations that  
534 best represent both local CO<sub>2</sub> flux patterns and regional atmospheric CO<sub>2</sub> enhancements. The simulated regional net CO<sub>2</sub> flux  
535 is highly sensitive to assumptions made while scaling up eddy flux observations, especially the ecosystem response to soil  
536 temperature of tundra during the cold season and the spatial distribution of tundra types across the North Slope. Additionally,  
537 scaling methods that average observations from multiple eddy covariance flux sites should consider which sites are most  
538 representative of the regional impact of the biosphere on the atmosphere using integrative top-down observations.

539 This work shows that year-round measurements of atmospheric CO<sub>2</sub> concentrations and fluxes across heterogeneous  
540 terrestrial and aquatic ecosystems are needed to represent the drivers of CO<sub>2</sub> fluxes from Arctic regions. Arctic ecosystems  
541 have the potential to accelerate warming if vast stores of carbon are released or buffer warming if increasing carbon uptake  
542 from vegetation occurs. All components of Arctic tundra ecosystems must be fully incorporated into earth system models to  
543 improve projections of future climate warming and associated carbon cycle feedbacks.



#### 544 **Data availability**

545 Data that support the findings of this study are available as listed below:

546 TVPRM NEE for all ensemble simulations: <https://doi.org/10.3334/ORNLDAAAC/1920>.

547 ICS, ICT, and ICH eddy flux tower observations: <http://aon.iab.uaf.edu/data>.

548 IVO, ATQ, BES, BEO, and CMDL eddy flux tower observations: <https://doi.org/10.18739/A2X34MS1B>.

549 NOAA BRW tower observations: <https://www.esrl.noaa.gov/gmd/dv/data/?site=brw>.

550 ARM-ACME V aircraft observations: <https://www.osti.gov/dataexplorer/biblio/dataset/1346549>.

551 ABoVE Arctic-CAP aircraft observations: <https://doi.org/10.3334/ORNLDAAAC/1658>.

552 NARR meteorology: <https://psl.noaa.gov/data/gridded/data.narr.html>.

553 ERA5 meteorology: <https://www.ecmwf.int/en/forecasts/dataset/ecmwf-reanalysis-v5>.

554 GOME-2 SIF: [https://avdc.gsfc.nasa.gov/pub/data/satellite/MetOp/GOME\\_F/](https://avdc.gsfc.nasa.gov/pub/data/satellite/MetOp/GOME_F/).

555 GOSIF: <https://globalecology.unh.edu/data/GOSIF.html>.

556 CSIF: <http://doi.org/10.6084/m9.figshare.6387494>.

557 CAVM vegetation map: <https://www.geobotany.uaf.edu/cavm/>.

558 RasterCAVM vegetation map: <https://dx.doi.org/10.17632/c4xj5rv6kv.1>.

559 ABoVE LC vegetation map: <https://doi.org/10.3334/ORNLDAAAC/1691>.

560 RS-PM soil temperature: available from authors upon request.

561 NOAA BRW tower and ARM-ACME V aircraft campaign WRF-STILT footprints:

562 <https://doi.org/10.3334/ORNLDAAAC/1431>, particle trajectories: <https://doi.org/10.3334/ORNLDAAAC/1430>.

563 ABoVE Arctic-CAP aircraft campaign WRF-STILT footprints: <https://doi.org/10.3334/ORNLDAAAC/1896>, particle

564 trajectories: <https://doi.org/10.3334/ORNLDAAAC/1895>.

565 Luus et al. (2017) fluxes: <https://doi.org/10.3334/ORNLDAAAC/1314>.

566 Commane et al. (2017) optimized fluxes: <https://doi.org/10.3334/ORNLDAAAC/1389>.

567 Natali & Watts et al. (2019) fluxes: <https://doi.org/10.3334/ORNLDAAAC/1683>.

568 Watts et al. (2021) fluxes: <https://doi.org/10.3334/ORNLDAAAC/1935>.

#### 569 **Author contributions**

570 LDS and RC designed the study. KAA, ESE, WCO, and DZ provided eddy covariance flux tower data. SCB, KM, and CS  
571 provided aircraft concentration data. JMH and MEM provided WRF-STILT particle files and footprints. YY provided RS-PM  
572 soil temperature data. JDW provided Watts et al. (2021) cold season belowground CO<sub>2</sub> fluxes. LDS developed and evaluated  
573 TVPRM net CO<sub>2</sub> fluxes against observations. RC, EJLL, JWM, and JDW assisted the analysis. LDS wrote the paper. All co-  
574 authors contributed to the preparation of the manuscript.



## 575 **Competing interests**

576 Authors declare that they have no competing interests.

## 577 **Acknowledgments**

578 We would like to acknowledge that the Alaskan North Slope is home to multiple Alaska Native nations, including the  
579 Nunamiut, Gwich'in, Koyukuk, and Iñupiaq peoples. We support and honor the place-based knowledge of Indigenous Peoples  
580 and recognize their ancestral and contemporary stewardship of their homelands that we research. LDS and RC are supported  
581 by research funding from the Department of Earth and Environmental Sciences at Columbia University and the NASA ABoVE  
582 grant #NNX17AC61A. LDS is additionally supported by the National Science Foundation (NSF) Office of Polar Programs  
583 grant #1848620. EJRL and JWM are supported by NASA ABoVE grant #NNX17AE75G. JDW is supported by NASA  
584 ABoVE grant #80NSSC19M0209 and NASA grant #NNH17ZDA001N-NIP. Part of the research was carried out at the Jet  
585 Propulsion Laboratory, California Institute of Technology, under a contract with NASA (80NM0018D0004). Imnavit Creek  
586 flux towers are funded under grants from the NSF Office of Polar Programs, 1503912 and 0632264. Resources supporting  
587 JMH and WRF-STILT modeling were provided by NASA grant #NNX17AE75G, #NNX17AC61A, and the NASA High-End  
588 Computing (HEC) Program through the NASA Advanced Supercomputing (NAS) Division at Ames Research Center. We  
589 thank the R Project community for analysis and plotting tools, especially the ggplot2, ggpattern, magick, anytime, lubridate,  
590 raster, and cowplot packages. NCEP Reanalysis data provided by the NOAA/OAR/ESRL PSL, Boulder, Colorado, USA.

## 591 **References**

- 592 Arndt, K. A., Oechel, W. C., Goodrich, J. P., Bailey, B. A., Kalhori, A., Hashemi, J., Sweeney, C., and Zona, D.: Sensitivity  
593 of Methane Emissions to Later Soil Freezing in Arctic Tundra Ecosystems, *J. Geophys. Res. Biogeosci.*, 124, 2595–2609,  
594 <https://doi.org/10.1029/2019JG005242>, 2019.
- 595 Arndt, K. A., Lipson, D. A., Hashemi, J., Oechel, W. C., and Zona, D.: Snow melt stimulates ecosystem respiration in Arctic  
596 ecosystems, *Global Change Biol.*, 26, 5042–5051, <https://doi.org/10.1111/gcb.15193>, 2020.
- 597 Bayer, T. K., Gustafsson, E., Brakebusch, M., and Beer, C.: Future Carbon Emission From Boreal and Permafrost Lakes Are  
598 Sensitive to Catchment Organic Carbon Loads, *J. Geophys. Res. Biogeosci.*, 124, 1827–1848,  
599 <https://doi.org/10.1029/2018JG004978>, 2019.
- 600 Beckebanze, L., Rehder, Z., Holl, D., Wille, C., Mirbach, C., and Kutzbach, L.: Ignoring carbon emissions from thermokarst  
601 ponds results in overestimation of tundra net carbon uptake, *Biogeosciences*, 19, 1225–1244, [https://doi.org/10.5194/bg-19-](https://doi.org/10.5194/bg-19-1225-2022)  
602 1225-2022, 2022.
- 603 Biraud, S., Mei, F., Flynn, C., Hubbe, J., Long, C., Matthews, A., Pekour, M., Sedlacek, A., Springston, S., Tomlinson, J., and  
604 Chand, D.: Campaign datasets for ARM Airborne Carbon Measurements (ARM-ACME-V), Oak Ridge National Lab.  
605 (ORNL), Oak Ridge, TN (United States). Atmospheric Radiation Measurement (ARM) Archive,  
606 <https://doi.org/10.5439/1346549>, 2016.



- 607 Bowling, D. R. and Massman, W. J.: Persistent wind-induced enhancement of diffusive CO<sub>2</sub> transport in a mountain forest  
608 snowpack, *J. Geophys. Res. Biogeosci.*, 116, G04006, <https://doi.org/10.1029/2011JG001722>, 2011.
- 609 Box, J. E., Colgan, W. T., Christensen, T. R., Schmidt, N. M., Lund, M., Parmentier, F.-J. W., Brown, R., Bhatt, U. S.,  
610 Euskirchen, E. S., Romanovsky, V. E., Walsh, J. E., Overland, J. E., Wang, M., Corell, R. W., Meier, W. N., Wouters, B.,  
611 Mernild, S., Mjaard, J., Pawlak, J., and Olsen, M. S.: Key indicators of Arctic climate change: 1971–2017, *Environ. Res. Lett.*,  
612 14, 045010, <https://doi.org/10.1088/1748-9326/aafc1b>, 2019.
- 613 Chang, R. Y.-W., Miller, C. E., Dinardo, S. J., Karion, A., Sweeney, C., Daube, B. C., Henderson, J. M., Mountain, M. E.,  
614 Eluszkiewicz, J., Miller, J. B., Bruhwiler, L. M. P., and Wofsy, S. C.: Methane emissions from Alaska in 2012 from CARVE  
615 airborne observations, *PNAS*, 111, 16694–16699, <https://doi.org/10.1073/pnas.1412953111>, 2014.
- 616 Commane, R., Lindaas, J., Benmergui, J., Luus, K. A., Chang, R. Y.-W., Daube, B. C., Euskirchen, E. S., Henderson, J. M.,  
617 Karion, A., Miller, J. B., Miller, S. M., Parazoo, N. C., Randerson, J. T., Sweeney, C., Tans, P., Thoning, K., Veraverbeke, S.,  
618 Miller, C. E., and Wofsy, S. C.: Carbon dioxide sources from Alaska driven by increasing early winter respiration from Arctic  
619 tundra, *PNAS*, 114, 5361–5366, <https://doi.org/10.1073/pnas.1618567114>, 2017.
- 620 Elder, C. D., Xu, X., Walker, J., Schnell, J. L., Hinkel, K. M., Townsend-Small, A., Arp, C. D., Pohlman, J. W., Gaglioti, B.  
621 V., and Czimczik, C. I.: Greenhouse gas emissions from diverse Arctic Alaskan lakes are dominated by young carbon, *Nature*  
622 *Clim. Change*, 8, 166–171, <https://doi.org/10.1038/s41558-017-0066-9>, 2018.
- 623 Euskirchen, E. S., Bret-Harte, M. S., Scott, G. J., Edgar, C., and Shaver, G. R.: Seasonal patterns of carbon dioxide and water  
624 fluxes in three representative tundra ecosystems in northern Alaska, *Ecosphere*, 3, art4, <https://doi.org/10.1890/ES11-00202.1>,  
625 2012.
- 626 Euskirchen, E. S., Bret-Harte, M. S., Shaver, G. R., Edgar, C. W., and Romanovsky, V. E.: Long-Term Release of Carbon  
627 Dioxide from Arctic Tundra Ecosystems in Alaska, *Ecosystems*, 20, 960–974, <https://doi.org/10.1007/s10021-016-0085-9>,  
628 2017.
- 629 Fisher, J. B., Sikka, M., Oechel, W. C., Huntzinger, D. N., Melton, J. R., Koven, C. D., Ahlström, A., Arain, M. A., Baker, I.,  
630 Chen, J. M., Ciais, P., Davidson, C., Dietze, M., El-Masri, B., Hayes, D., Huntingford, C., Jain, A. K., Levy, P. E., Lomas, M.,  
631 R., Poulter, B., Price, D., Sahoo, A. K., Schaefer, K., Tian, H., Tomelleri, E., Verbeeck, H., Viovy, N., Wania, R., Zeng, N.,  
632 and Miller, C. E.: Carbon cycle uncertainty in the Alaskan Arctic, *Biogeosciences*, 11, 4271–4288, <https://doi.org/10.5194/bg->  
633 11-4271-2014, 2014.
- 634 Goodrich, J. P., Oechel, W. C., Gioli, B., Moreaux, V., Murphy, P. C., Burba, G., and Zona, D.: Impact of different eddy  
635 covariance sensors, site set-up, and maintenance on the annual balance of CO<sub>2</sub> and CH<sub>4</sub> in the harsh Arctic environment, *Agr.*  
636 *Forest Meteorol.*, 228–229, 239–251, <https://doi.org/10.1016/j.agrformet.2016.07.008>, 2016.
- 637 Henderson, J. M., Eluszkiewicz, J., Mountain, M. E., Nehrkorn, T., Chang, R. Y.-W., Karion, A., Miller, J. B., Sweeney, C.,  
638 Steiner, N., Wofsy, S. C., and Miller, C. E.: Atmospheric transport simulations in support of the Carbon in Arctic Reservoirs  
639 Vulnerability Experiment (CARVE), *Atmos. Chem. Phys.*, 15, 4093–4116, <https://doi.org/10.5194/acp-15-4093-2015>, 2015.
- 640 Hersbach, H., Bell, B., Berrisford, P., Hirahara, S., Horányi, A., Muñoz-Sabater, J., Nicolas, J., Peubey, C., Radu, R., Schepers,  
641 D., Simmons, A., Soci, C., Abdalla, S., Abellan, X., Balsamo, G., Bechtold, P., Biavati, G., Bidlot, J., Bonavita, M., Chiara,  
642 G. D., Dahlgren, P., Dee, D., Diamantakis, M., Dragani, R., Flemming, J., Forbes, R., Fuentes, M., Geer, A., Haimberger, L.,  
643 Healy, S., Hogan, R. J., Hólm, E., Janisková, M., Keeley, S., Laloyaux, P., Lopez, P., Lupu, C., Radnoti, G., Rosnay, P. de,  
644 Rozum, I., Vamborg, F., Villaume, S., and Thépaut, J.-N.: The ERA5 global reanalysis, *Q. J. Roy. Meteorol. Soc.*, 146, 1999–  
645 2049, <https://doi.org/10.1002/qj.3803>, 2020.



- 646 Holgerson, M. A. and Raymond, P. A.: Large contribution to inland water CO<sub>2</sub> and CH<sub>4</sub> emissions from very small ponds,  
647 *Nat. Geosci.*, 9, 222–226, <https://doi.org/10.1038/ngeo2654>, 2016.
- 648 Hugelius, G., Strauss, J., Zubrzycki, S., Harden, J. W., Schuur, E. a. G., Ping, C.-L., Schirrmeister, L., Grosse, G., Michaelson,  
649 G. J., Koven, C. D., O'Donnell, J. A., Elberling, B., Mishra, U., Camill, P., Yu, Z., Palmtag, J., and Kuhry, P.: Estimated stocks  
650 of circumpolar permafrost carbon with quantified uncertainty ranges and identified data gaps, *Biogeosciences*, 11, 6573–6593,  
651 <https://doi.org/10.5194/bg-11-6573-2014>, 2014.
- 652 Jeong, S.-J., Bloom, A. A., Schimel, D., Sweeney, C., Parazoo, N. C., Medvigy, D., Schaepman-Strub, G., Zheng, C., Schwalm,  
653 C. R., Huntzinger, D. N., Michalak, A. M., and Miller, C. E.: Accelerating rates of Arctic carbon cycling revealed by long-  
654 term atmospheric CO<sub>2</sub> measurements, *Sci. Adv.*, 4, eaao1167, <https://doi.org/10.1126/sciadv.aao1167>, 2018.
- 655 Joiner, J., Yoshida, Y., Guanter, L., and Middleton, E. M.: New methods for the retrieval of chlorophyll red fluorescence from  
656 hyperspectral satellite instruments: simulations and application to GOME-2 and SCIAMACHY, *Atmos. Meas. Tech.*, 9, 3939–  
657 3967, <https://doi.org/10.5194/amt-9-3939-2016>, 2016.
- 658 Kim, Y., Kimball, J. S., Zhang, K., and McDonald, K. C.: Satellite detection of increasing Northern Hemisphere non-frozen  
659 seasons from 1979 to 2008: Implications for regional vegetation growth, *Remote Sens. Environ.*, 121, 472–487,  
660 <https://doi.org/10.1016/j.rse.2012.02.014>, 2012.
- 661 Kittler, F., Eugster, W., Foken, T., Heimann, M., Kolle, O., and Göckede, M.: High-quality eddy-covariance CO<sub>2</sub> budgets  
662 under cold climate conditions, *J. Geophys. Res. Biogeosci.*, 122, 2064–2084, <https://doi.org/10.1002/2017JG003830>, 2017.
- 663 Larson, E. J. L., Schiferl, L. D., Commane, R., Munger, J. W., Trugman, A. T., Ise, T., Euskirchen, E. S., Wofsy, S., and  
664 Moorcroft, P. M.: The changing carbon balance of tundra ecosystems: results from a vertically-resolved peatland biosphere  
665 model, *Environ. Res. Lett.*, 17, 014019, <https://doi.org/10.1088/1748-9326/ac4070>, 2021.
- 666 Li, X. and Xiao, J.: A Global, 0.05-Degree Product of Solar-Induced Chlorophyll Fluorescence Derived from OCO-2, MODIS,  
667 and Reanalysis Data, *Remote Sens.*, 11, 517, <https://doi.org/10.3390/rs11050517>, 2019.
- 668 Luus, K. A., Commane, R., Parazoo, N. C., Benmergui, J., Euskirchen, E. S., Frankenberg, C., Joiner, J., Lindaas, J., Miller,  
669 C. E., Oechel, W. C., Zona, D., Wofsy, S., and Lin, J. C.: Tundra photosynthesis captured by satellite-observed solar-induced  
670 chlorophyll fluorescence, *Geophys. Res. Lett.*, 44, 2016GL070842, <https://doi.org/10.1002/2016GL070842>, 2017.
- 671 Magney, T. S., Bowling, D. R., Logan, B. A., Grossmann, K., Stutz, J., Blanken, P. D., Burns, S. P., Cheng, R., Garcia, M. A.,  
672 Köhler, P., Lopez, S., Parazoo, N. C., Raczka, B., Schimel, D., and Frankenberg, C.: Mechanistic evidence for tracking the  
673 seasonality of photosynthesis with solar-induced fluorescence, *Proceedings of the National Academy of Sciences*, 116, 11640–  
674 11645, <https://doi.org/10.1073/pnas.1900278116>, 2019.
- 675 Magnússon, R. Í., Limpens, J., van Huissteden, J., Kleijn, D., Maximov, T. C., Rotbarth, R., Sass-Klaassen, U., and Heijmans,  
676 M. M. P. D.: Rapid Vegetation Succession and Coupled Permafrost Dynamics in Arctic Thaw Ponds in the Siberian Lowland  
677 Tundra, *J. Geophys. Res. Biogeosci.*, 125, 2019JG005618, <https://doi.org/10.1029/2019JG005618>, 2020.
- 678 Meredith, M., Sommerkorn, M., Cassotta, S., Derksen, C., Ekaykin, A., Hollowed, A., Kofinas, G., Mackintosh, A.,  
679 Melbourne-Thomas, J., Muelbert, M. M. C., Ottersen, G., Pritchard, H., and Schuur, E. A. G.: Polar Regions, in: IPCC Special  
680 Report on the Ocean and Cryosphere in a Changing Climate, edited by: Pörtner, H.-O., Roberts, D. C., Masson-Delmotte, V.,  
681 Zhai, P., Tignor, M., Poloczanska, E., Mintenbeck, K., Alegría, A., Nicolai, M., Okem, A., Petzold, J., Rama, B., and Weyer,  
682 N. M., 2019.



- 683 Mesinger, F., DiMego, G., Kalnay, E., Mitchell, K., Shafran, P. C., Ebisuzaki, W., Jović, D., Woollen, J., Rogers, E., Berbery,  
684 E. H., Ek, M. B., Fan, Y., Grumbine, R., Higgins, W., Li, H., Lin, Y., Manikin, G., Parrish, D., and Shi, W.: North American  
685 Regional Reanalysis, *B. Am. Meteorol. Soc.*, 87, 343–360, <https://doi.org/10.1175/BAMS-87-3-343>, 2006.
- 686 Miller, S. M., Miller, C. E., Commene, R., Chang, R. Y.-W., Dinardo, S. J., Henderson, J. M., Karion, A., Lindaas, J., Melton,  
687 J. R., Miller, J. B., Sweeney, C., Wofsy, S. C., and Michalak, A. M.: A multiyear estimate of methane fluxes in Alaska from  
688 CARVE atmospheric observations, *Global Biogeochem. Cycles*, 30, 1441–1453, <https://doi.org/10.1002/2016GB005419>,  
689 2016.
- 690 Natali, S. M., Watts, J. D., Rogers, B. M., Potter, S., Ludwig, S. M., Selbmann, A.-K., Sullivan, P. F., Abbott, B. W., Arndt,  
691 K. A., Birch, L., Björkman, M. P., Bloom, A. A., Celis, G., Christensen, T. R., Christiansen, C. T., Commene, R., Cooper, E.  
692 J., Crill, P., Czimeczik, C., Davydov, S., Du, J., Egan, J. E., Elberling, B., Euskirchen, E. S., Friborg, T., Genet, H., Göckede,  
693 M., Goodrich, J. P., Grogan, P., Helbig, M., Jafarov, E. E., Jastrow, J. D., Kalhori, A. A. M., Kim, Y., Kimball, J. S., Kutzbach,  
694 L., Lara, M. J., Larsen, K. S., Lee, B.-Y., Liu, Z., Lorant, M. M., Lund, M., Lupascu, M., Madani, N., Malhotra, A., Matamala,  
695 R., McFarland, J., McGuire, A. D., Michelsen, A., Minions, C., Oechel, W. C., Olefeldt, D., Parmentier, F.-J. W., Pirk, N.,  
696 Poulter, B., Quinton, W., Rezanezhad, F., Risk, D., Sachs, T., Schaefer, K., Schmidt, N. M., Schuur, E. A. G., Semenchuk, P.  
697 R., Shaver, G., Sonntag, O., Starr, G., Treat, C. C., Waldrop, M. P., Wang, Y., Welker, J., Wille, C., Xu, X., Zhang, Z.,  
698 Zhuang, Q., and Zona, D.: Large loss of CO<sub>2</sub> in winter observed across the northern permafrost region, *Nat. Clim. Change*,  
699 9, 852–857, <https://doi.org/10.1038/s41558-019-0592-8>, 2019.
- 700 Oechel, W. C., Laskowski, C. A., Burba, G., Gioli, B., and Kalhori, A. A. M.: Annual patterns and budget of CO<sub>2</sub> flux in an  
701 Arctic tussock tundra ecosystem, *J. Geophys. Res. Biogeosci.*, 119, 323–339, <https://doi.org/10.1002/2013JG002431>, 2014.
- 702 Outcalt, S. I., Nelson, F. E., and Hinkel, K. M.: The zero-curtain effect: Heat and mass transfer across an isothermal region in  
703 freezing soil, *Water Resour. Res.*, 26, 1509–1516, <https://doi.org/10.1029/WR026i007p01509>, 1990.
- 704 Pallandt, M. M. T. A., Kumar, J., Mauritz, M., Schuur, E. A. G., Virkkala, A.-M., Celis, G., Hoffman, F. M., and Göckede,  
705 M.: Representativeness assessment of the pan-Arctic eddy covariance site network and optimized future enhancements,  
706 *Biogeosciences*, 19, 559–583, <https://doi.org/10.5194/bg-19-559-2022>, 2022.
- 707 Porcar-Castell, A., Tyystjärvi, E., Atherton, J., van der Tol, C., Flexas, J., Pfündel, E. E., Moreno, J., Frankenberg, C., and  
708 Berry, J. A.: Linking chlorophyll a fluorescence to photosynthesis for remote sensing applications: mechanisms and challenges,  
709 *J. Exp. Bot.*, 65, 4065–4095, <https://doi.org/10.1093/jxb/eru191>, 2014.
- 710 Reynolds, M. K., Walker, D. A., Balser, A., Bay, C., Campbell, M., Cherosov, M. M., Daniëls, F. J. A., Eidesen, P. B.,  
711 Ermokhina, K. A., Frost, G. V., Jedrzejek, B., Jorgenson, M. T., Kennedy, B. E., Kholod, S. S., Lavrinenko, I. A., Lavrinenko,  
712 O. V., Magnússon, B., Matveyeva, N. V., Metúsalemsson, S., Nilsen, L., Olthof, I., Pospelov, I. N., Pospelova, E. B., Pouliot,  
713 D., Razzhivin, V., Schaepman-Strub, G., Šibík, J., Telyatnikov, M. Yu., and Troeva, E.: A raster version of the Circumpolar  
714 Arctic Vegetation Map (CAVM), *Remote Sens. Environ.*, 232, 111297, <https://doi.org/10.1016/j.rse.2019.111297>, 2019.
- 715 Romanovsky, V. E. and Osterkamp, T. E.: Effects of unfrozen water on heat and mass transport processes in the active layer  
716 and permafrost, *Permafrost Periglac.*, 11, 219–239, [https://doi.org/10.1002/1099-1530\(200007/09\)11:3<219::AID-  
717 PPP352>3.0.CO;2-7](https://doi.org/10.1002/1099-1530(200007/09)11:3<219::AID-PPP352>3.0.CO;2-7), 2000.
- 718 Schuur, E. A. G., McGuire, A. D., Schädel, C., Grosse, G., Harden, J. W., Hayes, D. J., Hugelius, G., Koven, C. D., Kuhry,  
719 P., Lawrence, D. M., Natali, S. M., Olefeldt, D., Romanovsky, V. E., Schaefer, K., Turetsky, M. R., Treat, C. C., and Vonk, J.  
720 E.: Climate change and the permafrost carbon feedback, *Nature*, 520, 171–179, <https://doi.org/10.1038/nature14338>, 2015.





- 721 Sun, Y., Frankenberg, C., Wood, J. D., Schimel, D. S., Jung, M., Guanter, L., Drewry, D. T., Verma, M., Porcar-Castell, A.,  
722 Griffis, T. J., Gu, L., Magney, T. S., Köhler, P., Evans, B., and Yuen, K.: OCO-2 advances photosynthesis observation from  
723 space via solar-induced chlorophyll fluorescence, *Science*, 358, eaam5747, <https://doi.org/10.1126/science.aam5747>, 2017.
- 724 Sweeney, C. and McKain, K.: ABoVE: Atmospheric Profiles of CO, CO<sub>2</sub> and CH<sub>4</sub> Concentrations from Arctic-CAP, 2017,  
725 ORNL DAAC, <https://doi.org/10.3334/ORNLDAAC/1658>, 2019.
- 726 Sweeney, C., Dlugokencky, E., Miller, C. E., Wofsy, S., Karion, A., Dinardo, S., Chang, R. Y.-W., Miller, J. B., Bruhwiler,  
727 L., Crotwell, A. M., Newberger, T., McKain, K., Stone, R. S., Wolter, S. E., Lang, P. E., and Tans, P.: No significant increase  
728 in long-term CH<sub>4</sub> emissions on North Slope of Alaska despite significant increase in air temperature, *Geophys. Res. Lett.*, 43,  
729 6604–6611, <https://doi.org/10.1002/2016GL069292>, 2016.
- 730 Sweeney, C., Chatterjee, A., Wolter, S., McKain, K., Bogue, R., Conley, S., Newberger, T., Hu, L., Ott, L., Poulter, B., Schiferl,  
731 L., Weir, B., Zhang, Z., and Miller, C. E.: Using atmospheric trace gas vertical profiles to evaluate model fluxes: a case study  
732 of Arctic-CAP observations and GEOS simulations for the ABoVE domain, *Atmospheric Chemistry and Physics*, 22, 6347–  
733 6364, <https://doi.org/10.5194/acp-22-6347-2022>, 2022.
- 734 Tadić, J. M., Miller, S., Yadav, V., and Biraud, S. C.: Greenhouse gas fluxes from Alaska's North Slope inferred from the  
735 Airborne Carbon Measurements Campaign (ACME-V), *Atmos. Environ.*, 118239,  
736 <https://doi.org/10.1016/j.atmosenv.2021.118239>, 2021.
- 737 Tan, Z., Zhuang, Q., Shurpali, N. J., Marushchak, M. E., Biasi, C., Eugster, W., and Anthony, K. W.: Modeling CO<sub>2</sub> emissions  
738 from Arctic lakes: Model development and site-level study, *J. Adv. Model. Earth Syst.*, 9, 2190–2213,  
739 <https://doi.org/10.1002/2017MS001028>, 2017.
- 740 Tao, J., Zhu, Q., Riley, W. J., and Neumann, R. B.: Warm-season net CO<sub>2</sub> uptake  
741 outweighs cold-season emissions over Alaskan North Slope tundra under current and RCP8.5 climate, *Environ. Res. Lett.*, 16,  
742 055012, <https://doi.org/10.1088/1748-9326/abf6f5>, 2021.
- 743 Walker, D. A., Reynolds, M. K., Daniëls, F. J. A., Einarsson, E., Elvebakk, A., Gould, W. A., Katenin, A. E., Kholod, S. S.,  
744 Markon, C. J., Melnikov, E. S., Moskalenko, N. G., Talbot, S. S., Yurtsev, B. A. (†), and Team, T. other members of the C.:  
745 The Circumpolar Arctic vegetation map, *J. Veg. Sci.*, 16, 267–282, <https://doi.org/10.1111/j.1654-1103.2005.tb02365.x>, 2005.
- 746 Wang, J. A., Sulla-Menashe, D., Woodcock, C. E., Sonnentag, O., Keeling, R. F., and Friedl, M. A.: Extensive land cover  
747 change across Arctic–Boreal Northwestern North America from disturbance and climate forcing, *Global Change Biol.*, 26,  
748 807–822, <https://doi.org/10.1111/gcb.14804>, 2020.
- 749 Watts, J. D., Natali, S. M., Minions, C., Risk, D., Arndt, K., Zona, D., Euskirchen, E. S., Rocha, A. V., Sonnentag, O., Helbig,  
750 M., Kalhori, A., Oechel, W., Ikawa, H., Ueyama, M., Suzuki, R., Kobayashi, H., Celis, G., Schuur, E. A. G., Humphreys, E.,  
751 Kim, Y., Lee, B.-Y., Goetz, S., Madani, N., Schiferl, L. D., Commane, R., Kimball, J. S., Liu, Z., Torn, M. S., Potter, S., Wang,  
752 J. A., Jorgenson, M. T., Xiao, J., Li, X., and Edgar, C.: Soil respiration strongly offsets carbon uptake in Alaska and Northwest  
753 Canada, *Environ. Res. Lett.*, 16, 084051, <https://doi.org/10.1088/1748-9326/ac1222>, 2021.
- 754 Worthy, D. E. J., Chan, E., Ishizawa, M., Chan, D., Poss, C., Dlugokencky, E. J., Maksyutov, S., and Levin, I.: Decreasing  
755 anthropogenic methane emissions in Europe and Siberia inferred from continuous carbon dioxide and methane observations  
756 at Alert, Canada, *J. Geophys. Res. Atmos.*, 114, <https://doi.org/10.1029/2008JD011239>, 2009.
- 757 Yang, X., Tang, J., Mustard, J. F., Lee, J.-E., Rossini, M., Joiner, J., Munger, J. W., Kornfeld, A., and Richardson, A. D.:  
758 Solar-induced chlorophyll fluorescence that correlates with canopy photosynthesis on diurnal and seasonal scales in a  
759 temperate deciduous forest, *Geophys. Res. Lett.*, 42, 2977–2987, <https://doi.org/10.1002/2015GL063201>, 2015.



- 760 Yi, Y., Kimball, J. S., Chen, R. H., Moghaddam, M., Reichle, R. H., Mishra, U., Zona, D., and Oechel, W. C.: Characterizing  
761 permafrost active layer dynamics and sensitivity to landscape spatial heterogeneity in Alaska, *Cryosphere*, 12, 145–161,  
762 <https://doi.org/10.5194/tc-12-145-2018>, 2018.
- 763 Yi, Y., Kimball, J. S., Chen, R. H., Moghaddam, M., and Miller, C. E.: Sensitivity of active-layer freezing process to snow  
764 cover in Arctic Alaska, *Cryosphere*, 13, 197–218, <https://doi.org/10.5194/tc-13-197-2019>, 2019.
- 765 Zhang, Y., Joiner, J., Alemohammad, S. H., Zhou, S., and Gentine, P.: A global spatially contiguous solar-induced fluorescence  
766 (CSIF) dataset using neural networks, *Biogeosciences*, 15, 5779–5800, <https://doi.org/10.5194/bg-15-5779-2018>, 2018.
- 767 Zhang, Y., Commane, R., Zhou, S., Williams, A. P., and Gentine, P.: Light limitation regulates the response of autumn  
768 terrestrial carbon uptake to warming, *Nat. Clim. Change*, 10, 739–743, <https://doi.org/10.1038/s41558-020-0806-0>, 2020.
- 769 Zona, D., Gioli, B., Commane, R., Lindaas, J., Wofsy, S. C., Miller, C. E., Dinardo, S. J., Dengel, S., Sweeney, C., Karion,  
770 A., Chang, R. Y.-W., Henderson, J. M., Murphy, P. C., Goodrich, J. P., Moreaux, V., Liljedahl, A., Watts, J. D., Kimball, J.  
771 S., Lipson, D. A., and Oechel, W. C.: Cold season emissions dominate the Arctic tundra methane budget, *PNAS*, 113, 40–45,  
772 <https://doi.org/10.1073/pnas.1516017113>, 2016.

773